MASTER

Delta-doped GaAs

Voncken, A.P.J.

Award date:
1989

δ-doped GaAs

A.P.J. Voncken
University of Technology Eindhoven
The Netherlands

December 7, 1989

Abstract

In this master thesis the electric properties of Si-δ-doped GaAs structures are investigated. These so called δ-dopes are M.B.E. grown GaAs structures which contain a sheet of donor atoms (Si) localized within several atomic layers. In practice diffusion and segregation effects can broaden the distribution. Provided moderately high dopant concentrations are present, a two-dimensional carrier gas is formed. The eigenstates of the confined carriers are subbands with energies which depend on the shape of the space-charge potential. Some basic properties of the δ-doped structures have been determined by magneto-transport measurements in magnetic fields up to 20 Tesla. The analyses of these measurements indicate that the GaAs substrate temperature during the growth is a very important system parameter. The structures grown at a temperature of 480^oC show an extremely narrow dopant profile ($\approx$ 20Å) which increases as the growth temperature is raised. An important mechanism causing the increase of the impurity spread at higher growth temperatures seems to be migration of Si-atoms with the growth front (segregation during growth). Segregation is also dependent on the areal impurity density as confirmed by SIMS measurements. The heavily doped structures show a large discrepancy between the number of Si-atoms in the dopant sheet and the number of donors determined from subband population measurements. It is not clear at the moment what mechanism is causing this discrepancy. For the lower dopant structures it is possible to calculate the different subband mobilities from measured quantities. The calculated mobilities can differ up to a factor four for the different subbands and are the highest mobilities reported thus far.

Contents

Chapter 1

The 2-D electron gas

Molecular Beam Epitaxy (M.B.E.) is potentially superior to conventional epitaxial techniques in the growth of very abrupt semiconducter transitions like $Al_xGa_{1-x}As/GaAs$ heterostructures and quantum wells. This technique is very suitable for growing very sharply confined doping layers, localized within several atomic layers, in bulk GaAs (δ-doping). Provided moderately high dopant concentrations are present (typical areal dopant concentrations are of the order $10^{12}/cm^2$), a two dimensional electron gas is formed. The critical areal dopant density(1) creating an 2-D electron gas is about 2 $10^{11}/cm^2$. A common feature of these structures is the formation of a multi subband electron gas at the dopant plane which has interesting electrical properties. A brief overview of electrical properties of two dimensional electron gases is presented in this chapter. The theoretical model used to perform numerical self-consistent calculations is discussed in the second chapter. The results of these calculations are presented in chapter 2 too. A more advanced theoretical analysis of the Shubnikov-de Haas and Hall signals of these structures is presented in chapter 3. In the fourth chapter we present the results and conclusions of the measurements performed on six samples.

1.1 Introduction

The scientific as well as the technological interest on III-V semiconductors nowadays is mainly concentrated on low-dimensional systems. These low-dimensional semiconductor systems can have very different electrical and optical properties, than observed in bulk materials. Realisation of these structures is only possible with highly developed epitaxial techniques like M.B.E. or M.O.C.V.D. (Metal Organic Chemical Vapour Epitaxy). A two dimensional system particulary of interest to us, is Si-δ-doped GaAs. A schematic diagram of this structure is given in figure 1.1. This structure consist of pure GaAs which contains an (atomic) sharply confined impurity sheet of silicon atoms. The typical background impurity concentration in M.B.E. grown GaAs is $10^{14}/cm^3$. Hence the main background impurity distance per atomic layer is approximately 0.3 μm. The Bohr-radius of Si-atoms in GaAs is, at zero temperature, circa 100Å. Only above a critical dopant concentration these Bohr-radii can have overlap, and a degenerated electron gas can arise. The expected insulator-metal transition occurs at an areal density of 2 $10^{11}/cm^2$. Above these densities the electrons are no longer confined to one donor only. And example of the Hartree potential the electrons "feel" is visualized in figure 1.2.

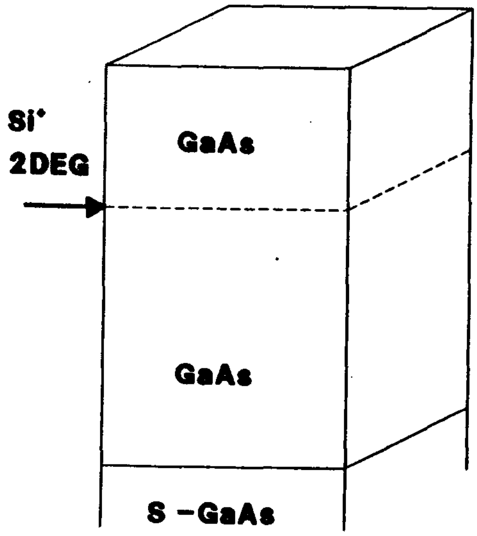

Figure 1.1 Schematic representation of a δ-doped structure.

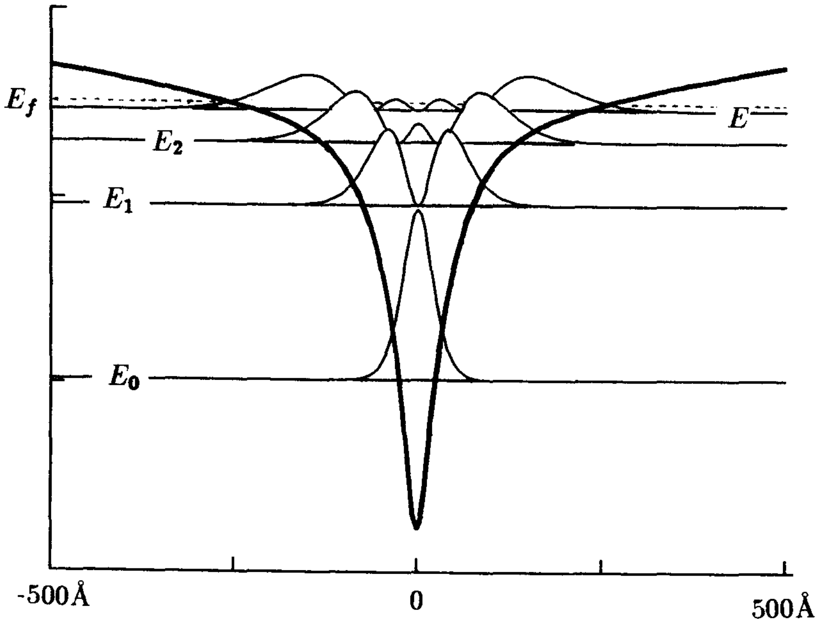

Figure 1.2 Typical form of the self-consistent calculated symmetric Hartree potential. This particular system has four subbands beneath the Fermi level. The probabilities of finding an electron at a distance z from the donor plane are also visualised. These probabilities are different in all subbands.

The different subband states have different probabilities of finding an electron at a distance z from the sheet of dopant. The electrons in the higher subbands tend to shift away from the plane of dopant while the lowest subband electrons have a maximum probability in the dopant plane. Thus we expect different subband mobilities at low temperatures since then ionized impurity scattering is the most important scattering mechanism. Part of this work consists of extracting the subband mobilities and the subband populations of these structures. This is done via magneto-transport measurements.

1.2 GaAs

1.2.1 Effective mass formalism

The effective mass formalism, introduced by Slater(2), states that the Schrödinger equation which describes all the electron states in the system can be replaced by a more simple equation. The idea is that the total system describing Schrödinger equation with a periodic potential can be replaced by a Schrödinger equation with an effective mass m^* and a smooth potential function. In case the effective mass is energy independent we have for bulk GaAs the following eigenvalue equation defining the electron states in the Γ-conduction band:

$$\frac{-\hbar^2}{2m^*}\left\{\frac{d^2}{dx^2}+\frac{d^2}{dy^2}+\frac{d^2}{dz^2}\right\}\phi(x,y,z)=E\phi(x,y,z) \tag{1.1}$$

with solutions

$$\phi(x,y,z)=exp(i\mathbf{k}\cdot\mathbf{r}) \tag{1.2}$$

where **k** represents the wave vector. The corresponding dispersion relation (E-k relation) becomes

$$E(\mathbf{k})=\frac{\hbar^2}{2m^*}(k_x^2+k_y^2+k_z^2) \tag{1.3}$$

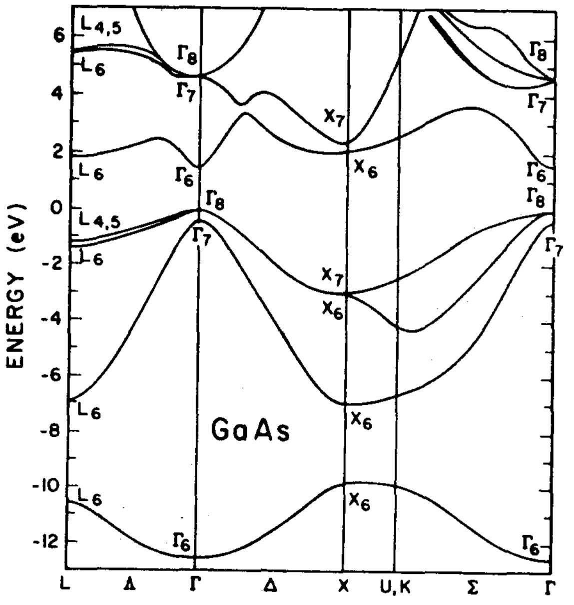

Figure 1.3a Electron energy vs reduced wave vector, for the four valence bands, and the first several conduction bands.

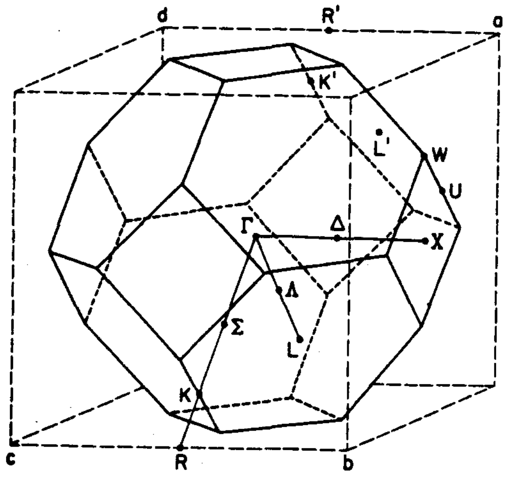

Figure 1.3b First Brillouin zone for the GaAs lattice.

This is the ideal (parabolic and isotropic) dispersion relation for electrons in the conduction band in GaAs. This relation is only valid for small values of k. At higher energies a more complex relation between the energy and the wave vector occurs as can be seen from figure 1.3a. This figure shows the dispersion relation in GaAs for various k-values and orientations.

For convenience the different k-orientations are visualized in figure 1.3b. An electron can not have a perfectly defined k-vector, but has always a small uncertainty $\Delta\mathbf{k}$ which gives rise to a wave-packet instead of the plane wave $exp(i\mathbf{k}\cdot\mathbf{r})$. The velocity of a wave packet that describes an electron state at a point $\mathbf{k}$ is given by

$$\mathbf{v} = \frac{1}{\hbar}\frac{\partial E(\mathbf{k})}{\partial \mathbf{k}} \tag{1.4}$$

Here $\hbar\mathbf{k} = \mathbf{p}$ does play the role of the classical momentum. In the presence of an electric field $\mathbf{E}$, we have $\hbar\dot{\mathbf{k}} = e\mathbf{E}$. When combining these two equations, we can calculate the acceleration of an electron,

$$\dot{\mathbf{v}} = \frac{\partial}{\partial t}\{\frac{1}{\hbar}\frac{\partial E(\mathbf{k})}{\partial \mathbf{k}}\} = \frac{1}{\hbar}\frac{\partial}{\partial \mathbf{k}}\{\frac{1}{\hbar}\frac{\partial E(\mathbf{k})}{\partial \mathbf{k}}\}\cdot\frac{\hbar\partial\mathbf{k}}{\partial t} \tag{1.5}$$

This finally gives:

$$\dot{\mathbf{v}} = \frac{1}{\hbar^2}\frac{\partial^2 E(\mathbf{k})}{\partial\mathbf{k}\partial\mathbf{k}}e\mathbf{E} \tag{1.6}$$

If we compare this with the conventional Newtionian equation

$$m\dot{\mathbf{v}} = e\mathbf{E} \tag{1.7}$$

we see that the equivalent of the mass of an electron is now the inverse of a tensor;

$$\frac{1}{m_{ij}} \longrightarrow \frac{1}{\hbar^2}\frac{\partial^2 E(\mathbf{k})}{\partial k_i \partial k_j} \tag{1.8}$$

This tensor is the nearest equivalent to a dynamical mass for the electron. For example, in a semiconductor the energy surface may be of the form

$$E(\mathbf{k}) = \frac{\hbar^2 k_1^2}{2m_1} + \frac{\hbar^2 k_2^2}{2m_2} + \frac{\hbar^2 k_3^2}{2m_3} \tag{1.9}$$

referred to some local principal axes. The effect of an electric field in accelerating an electron will then be very different in different directions.

1.2.2 Density of states and Fermi level

An important quantity in a semiconductor is the density of states function, which describes the number of electron states per energy interval as function of the energy. The density of states is closely related to the dispersion relation of the semiconductor. For a parabolic isotropic conduction band the two dimensional density of states function, $DOS_2(E)$, can be calculated from

$$DOS_2(E_2)dE = \sum_{\Delta\mathbf{k}} \frac{2}{(2\pi)^2} \tag{1.10}$$

where the summation runs over all $\Delta\mathbf{k}$ combinations obeying: $E(\mathbf{k}) = E_2; E(\mathbf{k}+\Delta\mathbf{k}) = E_2 + dE$. Appendix B shows how exactly the function $DOS_2(E)$ can be calculated from this equation. For a parabolic isotropic dispersion relation we then have:

$$DOS_2(E) = \frac{m^*}{\pi\hbar^2} \tag{1.11}$$

and for the three dimensional analogue

$$DOS_3(E) = \frac{1}{2\pi^2}(\frac{2m^*}{\hbar^2})^{\frac{3}{2}}\sqrt{E} \tag{1.12}$$

If however we use a parabolic an-isotropic dispersion relation like

$$E(\mathrm{k}) = \frac{\hbar^2 k_x^2}{2m_1} + \frac{\hbar^2 k_y^2}{2m_2} + \frac{\hbar^2 k_z^2}{2m_3} \tag{1.13}$$

both the density of states functions change and the effective mass is replaced by $m^* \longrightarrow \sqrt[3]{m_1 m_2 m_3}$ and $m^* \longrightarrow \sqrt{m_1 m_2}$ for the 3-D and 2-D situation respectively. This is sometimes used as the definition of the effective mass for a an-isotropic dispersion relation. A general equation for calculating from arbitrary dispersion relations the 2-D or 3-D density of states functions is given in appendix B.

The total density of electrons, n, can now be calculated via

$$n = \int_0^\infty f(E,T,E_f)\; DOS(E)\, dE \tag{1.14}$$

where $f(E,T,E_f)$ is the Fermi-Dirac distribution function and E_f the Fermi energy. At zero temperature this equation reduces to

$$n = \int_0^{E_f} DOS(E)\, dE \tag{1.15}$$

which is a mathematical formulation of the definition of the Fermi level.

1.3 2-D electron gases

In this section we shall give a short overview of important electrical properties of 2-dimensional electron gases. For a more detailed analysis of the presented formulae we refer to the reference list (3–5).

1.3.1 Transport properties of a one subband system

In the absence of a magnetic field the isothermal conductivity is defined as

$$\sigma_{xx}(0) = J_x/E_x = \frac{ne^2}{m^*} < \tau > \tag{1.16}$$

Here is J_x the electric current in the x-direction, E_x the electric field in the x-direction and $< \tau >$ the averaged scattering time. For a 2DEG at sufficiently low temperatures we can replace $< \tau >$ by the scattering time at the Fermi level $\tau(E_f)$. The drift mobility, μ_d, is defined as

$$\mu_d = \frac{e}{m^*} < \tau > = \frac{e}{m^*}\, \tau(E_f) \tag{1.17}$$

The drift mobility only depends on the scattering of electrons at the Fermi level. In the presence of a perpendicular magnetic field B we have the following relation between the electric current J and the electric field E

$$\mathbf{J} = \overline{\overline{\sigma}}\, \mathbf{E} \tag{1.18}$$

and via the inverse tensor relation

$$\mathbf{E} = \bar{\bar{\rho}}\,\mathbf{J} \tag{1.19}$$

where σ is the conductivity and ρ the resistivity tensor. The Hall constant, R_{Hall}, and the Hall mobility, μ_{Hall} are defined as

$$R_{Hall} = \frac{E_y}{J_x\,B} = \frac{1}{n\,e}\,\frac{<\tau^2>}{<\tau>^2} \tag{1.20}$$

and

$$\mu_{Hall} = \sigma_{xx}(0)\,|R_{Hall}| \tag{1.21}$$

respectively. For a one subband system at low temperatures the Hall constant reduces to $\frac{-1}{n\,e}$ and hence the Hall mobility equals the drift mobility μ_d. In the presence of a perpendicular magnetic field the density of states function, $DOS_2(E)$, changes dramatically from a constant to a set of delta-functions. This is visualized in figure 1.4. The electrons in the energy interval $(n+\frac{1}{2}\pm\frac{1}{2})\ \hbar eB/2m^*$ are all compressed to an energy $n\ \hbar eB/m^*$; here n is the Landau number. Every Landau level has a degeneracy, G, which is proportional to the magnetic field B i.e. $G = eB/\pi\hbar$. At absolute zero the Fermi level is pinned to the upper most filled Landau level. If the magnetic field is increased a little, the Fermi level will stay pinned to the highest filled Landau level untill this Landau level accomodates no more electron states. At that particular magnetic field the Fermi level will skip to the new top most filled Landau level. The Fermi energy skips periodically in 1/B, with a period S given by: $S = e/\pi\hbar N_{2DEG}$ where N_{2DEG} is the areal elctron density. Figure 1.5 shows how the Fermi level varies as the magnetic field is raised.

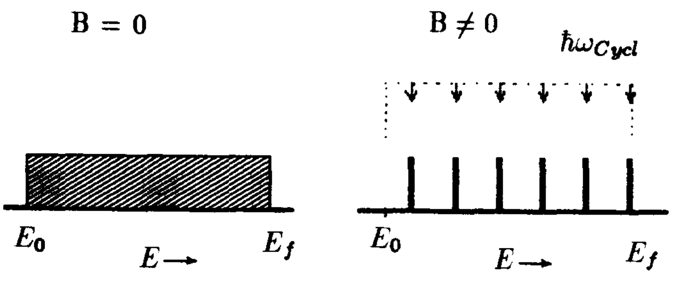

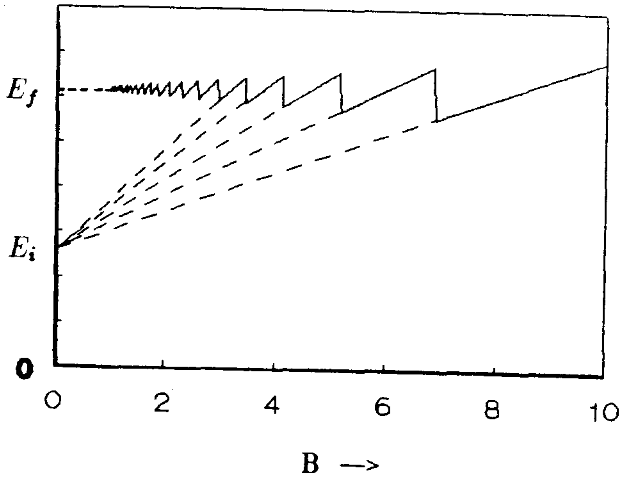

Figure 1.4 Change of the density of states function of a 2-D electron gas in the presence of a magnetic field.

Figure 1.5 Fermi level of a 2DEG as a function of the magnetic field at zero temperature in case spin-splitting is neglected.

At non zero temperatures the Fermi level changes more gradually. The periodicity of the Fermi level in the reciprocal magnetic field affects all other quantities of the system. For instance the resistivity will oscillate in 1/B with the same periodicity S. Measuring the periodicity in 1/B, directly gives the areal electron density of the system.

1.3.2 Transport properties of a multi-subband system

In the former subsection the Hall constant, R_{Hall}, was magnetic field independent. This no longer holds when we have more than one type of carriers present. For instance a multi subband 2DEG must be regarded as having different electron "types". The scattering time, τ_n, usually differs for electrons in different subbands. For a two subband system we then obtain for the Hall "constant"

$$R_{Hall} = \frac{R_1\sigma_1^2(1+\sigma_2^2B^2R_2^2) + R_2\sigma_2^2(1+\sigma_1^2B^2R_1^2)}{(\sigma_1+\sigma_2)^2 + \sigma_1^2\sigma_2^2B^2(R_1+R_2)} \tag{1.22}$$

where $R_i = \frac{-1}{n_i e}$ and $\sigma_i = n_i e\mu_i$. This equation is generally true even when τ is a function of v and for any two kinds of carriers, electrons and/or holes. Neglecting the terms in B^2 we have

$$R_{Hall} = \frac{R_1\sigma_1^2 + R_2\sigma_2^2}{(\sigma_1+\sigma_2)^2} \tag{1.23}$$

For a 2-dimensional electron gas we can rewrite this to

$$R_{Hall} = \frac{-1}{n_{Hall}e} = \frac{-1}{e}\{\frac{n_1\mu_1^2 + n_2\mu_2^2}{(n_1\mu_1+n_2\mu_2)^2}\} \tag{1.24}$$

which defines the Hall areal electron density, n_{Hall}. The Hall mobility, μ_{Hall}, follows from

$$\mu_{Hall} = (\sigma_1+\sigma_2)|R_{Hall}| = \frac{n_1\mu_1^2 + n_2\mu_2^2}{(n_1\mu_1+n_2\mu_2)} \tag{1.25}$$

Both the Hall mobility as the Hall areal electron density can be measured via Van de Pauw measurements. The general low field formulae for μ_{Hall} and n_{Hall} in a multi subband system are

$$n_{Hall} = \frac{(\sum_i n_i\mu_i)^2}{\sum_j n_j\mu_j^2} \tag{1.26}$$

$$\mu_{Hall} = \frac{\sum_j n_j\mu_j^2}{\sum_i n_i\mu_i} \tag{1.27}$$

Once these quantities have been measured, together with the different values of the subband populations, n_i, one can use these formulae to calculate the different subband mobilities μ_i. For more than two subbands however one can only approximate the mobilities of the different subbands, because there are still to many unknown parameters in our equations, assuming that n_{Hall}, n_i and μ_{Hall} have all been determined. In the presence of a perpendicular magnetic field, B, the density of states of the different subband are affected in the same way as explained in the former subsection. The total density of states for a three subband system in the presence of a magnetic field, B, is visualized in figure 1.6. Figure 1.7 shows how the

Fermi level is affected by the magnetic field at zero temperature.

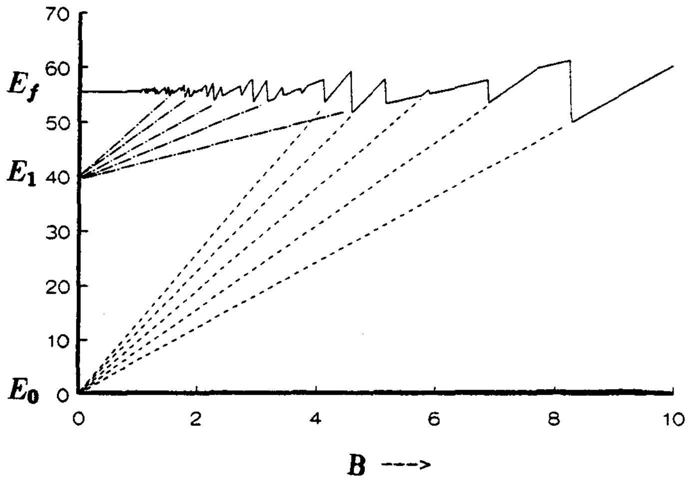

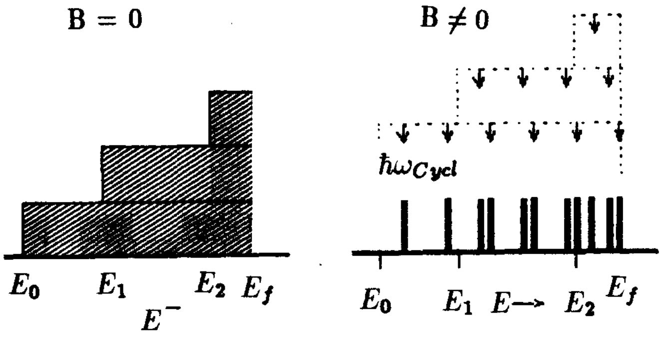

Figure 1.6 Change of the density of states function of a multi subband 2DEG in the presence of a magnetic field.

Figure 1.7 Fermi level of a (three subband) 2DEG as a function of the magnetic field at zero temperature in case spin-splitting is neglected.

We can notice again the jumps the Fermi level makes when a certain Landau level is depopulated. The periodicity of the Fermi level in 1/B is now a combination of three different subband periodicities, S_i, which again are proportional to $1/n_i$. So for a multi subband system the resistivity will also have oscillations, however more complex and with different periodicities than a one subband system. In chapter three we will examine in more detail the oscillatory behaviour of the resistivity.

1.4 Cyclotron resonance

The effect of a magnetic field on an electron state is given by

$$\dot{\mathbf{k}} = \frac{e}{\hbar}\mathbf{v} \times \mathbf{B} \tag{1.28}$$

This means that the change in the vector **k** is normal to the direction of **B** and normal to **v**. The velocity **v** itself is normal to the energy surface. Thus, **k** must be confined to an orbit defined by the section of the Fermi surface with the plane normal to **B**. The magnetic field simply drives the presentative point round this orbit without change of energy. If the electron is not scattered, it makes a circuit in the period

$$\frac{2\pi}{\omega_{cycl}} = \frac{eB}{\hbar}\oint\frac{dk}{v_\perp} \tag{1.29}$$

where $v_\perp$ is the component of **v** in the plane normal to **B** at a point **k**. The corresponding frequency, ω_{cycl}, is called the cyclotron frequency. For free electrons we have

$$\oint\frac{dk}{v_\perp} = \frac{m}{\hbar}\oint\frac{dk}{k_\perp} = \frac{2\pi m}{\hbar} \tag{1.30}$$

so that $\omega_{cycl} = \frac{eB}{m}$. It is customary to define the cyclotron effective mass such that

$$m^*_{cycl} = \frac{eB}{\omega_{cycl}} \tag{1.31}$$

It should be noted that this is not the same as the dynamical mass of the electron. It is a property of an orbit, not of a particular electron state. Using equation (1-29) finally gives

$$m^*_{cycl} = \frac{\hbar^2}{2\pi} \oint \frac{dk}{\|\nabla_k E\|} = \frac{\hbar^2}{2\pi} \frac{\partial \mathcal{A}}{\partial E} \tag{1.32}$$

where $\mathcal{A}$ is the area enclosed by the orbit in the plane normal to the magnetic field. For a two dimensional isotropic parabolic dispersion relation like

$$E(k_x, k_y) = \frac{\hbar^2}{2m^*}(k_x^2 + k_y^2) \tag{1.33}$$

the corresponding effective cyclotron mass, m^*_{cycl} is equal to the effective mass of conduction band m^*. This is easily verified. For a non-parabolic an-isotropic two dimensional dispersion relation they need not necessarily be the same. The effective cyclotron mass in the two dimensional situation however is proportional to the density of states function at the Fermi level. The periodic motion of the electrons could be detected by resonance with an electromagnetic field of suitable frequency. The only condition is that the electron should make at least one circuit of the orbit before being scattered. One therefore must measure at low temperatures and at sufficiently high magnetic fields in order to see an absorption peak.

1.5 Scattering mechanism

The electrons in the 2-D electron gas can be scattered by the irregular potentials in the crystal. The irregularities may come from the ionized impurities in the 2-D layer or in the GaAs and or the lattice vibrations (acoustic or polar optical phonons). Being governed by the Bose-Einstein distribution function, the population of phonons increases exponentially with temperature. At room temperature, the optical phonon states are so significally populated that they dominate the electron scattering processes. The longitudinal optical phonon energy for GaAs is 36 meV (410 K). At lower temperatures ionized impurity scattering through coulomb interaction is dominant. Figure 1.8 shows the temperature dependence of the mobility for different scattering mechanism.

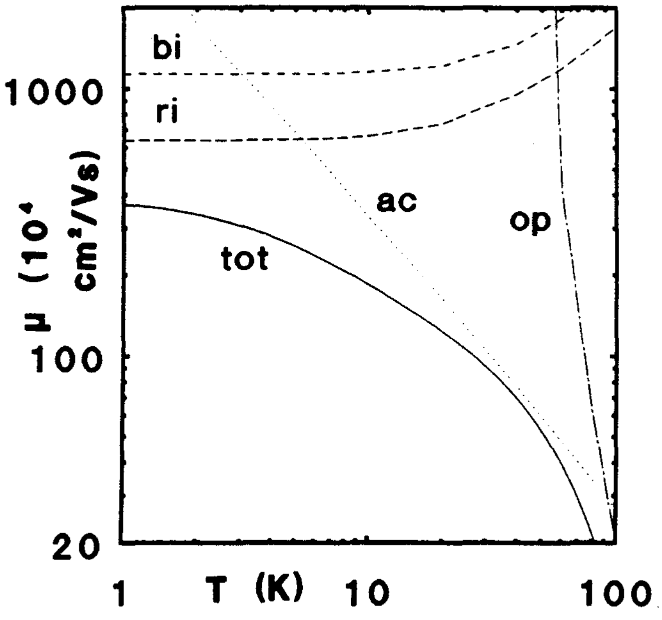

Figure 1.8 This figure shows the temperature dependence of the typical scattering mechanisms in the two dimensional electron gas in a hetero structure. For a δ-dope structure the different mobilities have other weight factors.

Figure 1.9 Figure showing typical curves of the temperature dependence of the mobility for a heterostructure, bulk GaAs, and a δ-doped structure.

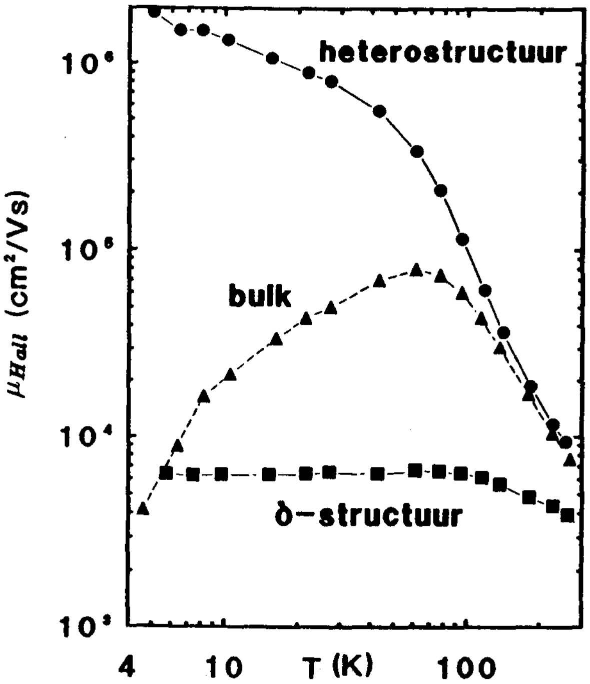

Note that the total mobility is calculated from

$$\frac{1}{\mu_{tot}} = \sum_i \frac{1}{\mu_i} \tag{1.34}$$

where μ_i represents the mobility due to one type of scattering mechanism. For a multi subband system this formula holds for each subband seperately. The systems mobility must be calculated from equation 1.27. For a more detailed analyses of these types of scattering mechanism see reference 6.

Chapter 2

Self-consistent calculations

It is a physical impossibility to create a system containing particles which can move (freely) in an infinitely thin layer. According to the Heisenberg uncertainty relation $\Delta z \Delta p_z \geq \hbar$ every particle will have an uncertainty in all its space coordinates as in the corresponding momentum coordinates. Thus there will always be a certain thickness or speading of the so called "two dimensional" system. In most cases however these quasi 2D systems can be described very well as being perfect 2D systems. The two dimensional electron gas (2DEG) is one of todays most investigated quasi 2D system (the hetero structures and quantum wells). Several authors have recently reported numerical calculations on the electronic subband structure in Si δ-doped GaAs systems(1,7–9). In our calculations we will follow the stategy introduced by Zrenner(1). In the first part of this chapter (section 2.1) we present the theory which is used to describe the equilibrium state of a Si δ-doped GaAs system at zero temperature. This (envelope-function) formalism however is a general theory not specifically derived for GaAs systems. In the second part (section 2.2) we present the results of the self consistent calculations performed on a IBM RT PC. Only a selected part of the calculations are presented in this report: The main part of the calculations are collected and depicted in an additional manual(10).

2.1 Theoretical description of δ-doped GaAs

2.1.1 One dimensional electron gas

Consider a free electron gas in one dimension that is confined to a length L by infinite barriers. The electron wave functions $\psi_n(z)$ are solutions of the Schrödinger equation $\mathcal{H}\ \psi_n(z) = E_n\ \psi_n(z)$; with neglect of potential energy we have $\mathcal{H} = p^2/2m$, where p is the momentum. In quantum theory p represents the operator $-i\hbar\ d/dz$ so that

$$\mathcal{H}\psi_n(z) = -\frac{\hbar^2}{2m}\ \frac{d^2}{dz^2}\psi_n(z) = E_n\ \psi_n(z) \tag{2.1}$$

where E_n is the energy of the electron described by wave function $\psi_n(z)$. The boundary conditions of this differential equation are $\psi_n(0) = 0$ and $\psi_n(L) = 0$. Proper normalization [1]

---

[1] $\int_0^L \psi_n(z)\ \psi_n^\dagger(z)\ dz = 1$

will give sinelike wave functions

$$\psi_n(z) = \sqrt{\frac{2}{L}} \sin(\frac{n\pi z}{L}) \tag{2.2}$$

and energy

$$E_n = \frac{\hbar^2}{2m} (\frac{n\pi}{L})^2 \tag{2.3}$$

In a linear solid the quantum numbers of an electron are n and m_s the spin quantum number which can take the values $\pm\frac{1}{2}$. According to the Pauli exclusion principle no two electrons can have identical quantum numbers. A quantum state labeled by quantum number n hence can accomodate only two electrons, one with spin up and one with spin down. This is called a (two fold) degeneracy. To accomodate N electrons in this one dimensional system the first $N/2$ energy levels must be filled with each two electrons. It is convenient to suppose that N is even. The Fermi energy E_f is defined as the topmost filled energy level in the ground state i.e. the $N/2^e$ energy level.

$$E_f = \frac{\hbar^2}{2m} (\frac{N\pi}{2L})^2 \tag{2.4}$$

The example of an infinite potential well resulted in rather simple solutions for the Schrödinger equation. However solving this eigen value equation may become an arduous task when a more complex potential function $U(z)$ enters the Schrödinger equation. In general the Schrödinger equation of a free electron gas feeling a potential $U(z)$ can be written as a set of non-linear (coupled) differential equations with four adequate boundary conditions:

$$\frac{d}{dz}\begin{pmatrix} \psi_n(z) \\ \phi_n(z) \\ E_n \\ N(z) \end{pmatrix} = \begin{pmatrix} \phi_n(z) \\ \frac{2m}{\hbar^2}(U(z) - E_n)\cdot\psi_n(z) \\ 0 \\ \psi_n(z)\psi_n(z) \end{pmatrix} \tag{2.5}$$

The first two boundary conditions are $N(-\infty) = 0$ and $N(\infty) = 1$ while the other two depend on the problem being addressed.

2.1.2 Model specification

A Si δ-doped GaAs system can best be characterized with the help of figure 2.1. This figure shows the energy band diagram of three parts of the δ-dope in case the heavily doped part is separated from the two enclosing GaAs layers. The GaAs in all the three parts is supposed to be slightly and uniformly doped with acceptors with a typical concentration N_{Acc} of order 10^{14} /cm^3. The acceptor levels are all supposed to lie at an energy E_{Acc} above the valence band. The midpart however is supposed to be also uniformly doped with Si donors[2] with a concentration N_d over a distance d_{Don}. These donor levels all lie at an energy E_{Don} below the conduction band. At zero temperature the Fermi level E_f (read chemical potential) in the midpart is different from that of the enclosing GaAs layers. When the separations are lifted, one expects the electrons with the highest chemical potential to drift to regions with lower chemical potential.[3] Due to the building up of a charge distribution $\rho(z)$ the potential

---

[2] The silicon atoms can only act as donors if they replace galium atoms in the lattice.

[3] In fact this can only happen at temperature above absolute zero; what is meant here is that the temperature is raised before the junction and brought back to zero afterwards.

function $U(z)$ will change shape and finally result in a "well shaped" function visualized in figure 2.2. The acceptor depletion region spreads out on both sides of the $z = 0$ plane over a distance d_{Acc}. In this region we assume all acceptors to be ionized. The Fermi level in the neutral GaAs (the undepleted regions $|z| > d_{Acc}$) lies $E_{Acc}/2$ above the valence band. Solving the Poisson equation in this region gives

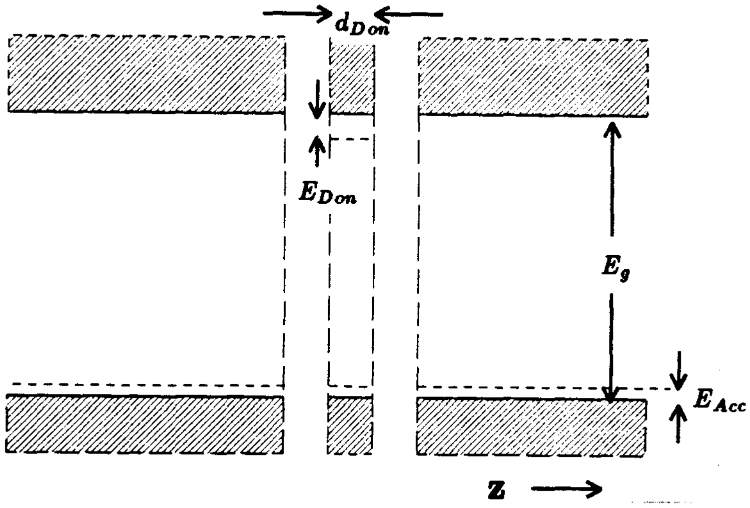

Figure 2.1 Schematic energy band diagram in case the heavily doped part is separated from the enclosing two GaAs layers.

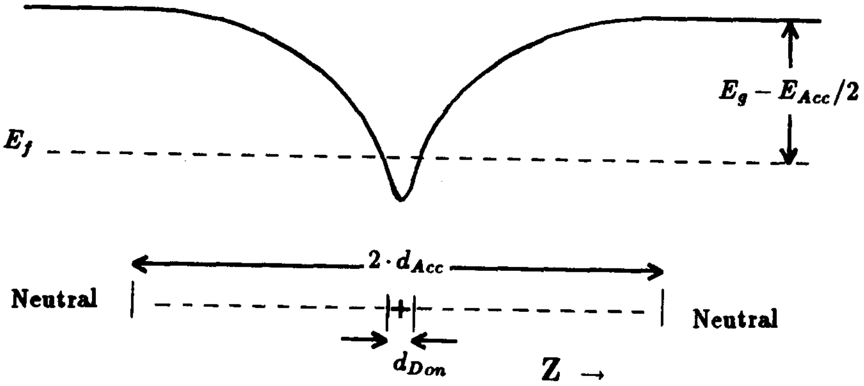

Figure 2.2 Schematic diagram showing the different space charge regions in the δ-dope system.

$$U(z) - E_f = E_g - E_{Acc}/2 \quad \text{for} \quad |z| \geq d_{Acc} \tag{2.6}$$

where E_g is the GaAs band gap at absolute zero.

2.1.3 System description

The potential energy function $U(z)$ for the electrons depends only on the coordinate perpendicular to the Si doped plane. The three-dimensional Schrödinger equation (2-7) defining the electron envelope functions $\Phi_n(x, y, z)$

$$-\frac{\hbar^2}{2m^*} \left(\frac{d^2}{dx^2} + \frac{d^2}{dy^2} + \frac{d^2}{dz^2} \right) \Phi_n(x, y, z) = \left(\mathcal{E}_n - U(z) \right) \Phi_n(x, y, z) \tag{2.7}$$

reduces to a one-dimensional Schrödinger equation (2-9) when a constant effective mass m^* is assumed. Envelope functions like

$$\Phi_{n,k_x,k_y}(x, y, z) = \phi_n(z) e^{i(k_x x + k_y y)} \tag{2.8}$$

finally give

$$\left(-\frac{\hbar^2}{2m^*}\frac{d^2}{dz^2}+U(z)-E_n\ \right)\phi_n(z)=0 \tag{2.9}$$

with

$$\mathcal{E}_n=E_n+\frac{\hbar^2(k_x^2+k_y^2)}{2m^*} \tag{2.10}$$

The quantum numbers necessary to characterize an electron state are: the (rather trivial and here omitted) spin quantum number m_s, the wave vectors k_x and k_y and the energy state index n. The wave vectors k_x and k_y are correct quantum numbers since the momentum operators p_x and p_y commute with the system's Hamiltonian (xy-plane symmetry). The energy eigen-functions Φ_{n,k_x,k_y} are simultaneously eigen-functions of the momentum operators p_x and p_y but no longer eigen-functions of the operator p_z. Hence the wave vector k_z is no quantum number. The kinetic energy T of electrons in a state $\Phi_{k_x,k_y,n}$ is given by

$$T_{k_x,k_y,n}=<\Phi_{n,k_x,k_y}|T_{op}|\Phi_{n,k_x,k_y}>=\frac{\hbar^2}{2m^*}(k_x^2+k_y^2+\int_{-\infty}^{\infty}|\tfrac{d}{dz}\phi_n(z)\ |^2dz\ ) \tag{2.11}$$

In bulk GaAs an electron in the conduction band can move "freely" in three dimensions with a kinetic energy

$$T=\frac{\hbar^2}{2m^*}(k_x^2+k_y^2+k_z^2) \tag{2.12}$$

In analogy to the situation in bulk GaAs we define a mean k_z as

$$<k_z>_n=\sqrt{<\Phi_{n,k_x,k_y}|\frac{d^2}{dz^2}|\Phi_{n,k_x,k_y}>}=\sqrt{\int_{-\infty}^{\infty}|\tfrac{d}{dz}\phi_n(z)\ |^2dz} \tag{2.13}$$

The importance of being able to define some sort of average k_z wave vector per energy subband is the fact that this mean $<k_z>_n$ value must be treated as a constant in the dispersion relation of bulk GaAs(11) which normally is k_x, k_y, k_z dependent. With this reduced dispersion relation (only the k_x and k_y dependency remains) one can calculate the corresponding 2-dimensional density of states DOS_2. How exactly this can be done is worked out in appendix B. For an isotropic parabolic dispersion relation like

$$E(\mathrm{k})=\tfrac{\hbar^2}{2m^*}(k_x^2+k_y^2+k_z^2) \tag{2.14}$$

the two dimensional density of states becomes

$$DOS_2(E)=\frac{m^*}{\pi\hbar^2} \tag{2.15}$$

In case the non-parabolic dispersion relation(11) is used, the density of states becomes

$$DOS_2(E,k_z)=\alpha(k_z)+\beta(k_z)\cdot E \tag{2.16}$$

with

$$\alpha(k_z)=\frac{m^*}{\pi\hbar^2}(0.993+2.46\ 10^{-19}k_z^2) \tag{2.17}$$

$$\beta(k_z)=\frac{m^*}{\pi\hbar^2}(1.52\ 10^{-3}+6.32\ 10^{-22}k_z^2) \tag{2.18}$$

Here the energy values are expressed in meV's and the wave vector k_z has dimension 1/m.

The electrons feel a potential $U(z)$ which consists of two contributions: a Hartree potential $U_C(z)$ and a part $U_X(z)$ which incorporates the exchange and correlation effects of the electron gas. We will use the exchange and correlation potential given by Gunnarson and Lundqvist$^{(12)}$

$$U_X(z) = -\sqrt[3]{\tfrac{18}{\pi^2}}\ \frac{m^* Ry}{m_e \epsilon_r^2 r_s}\ (1 + 0.0545\ r_s \ln(1 + \tfrac{11.4}{r_s})\ ) \tag{2.19}$$

where Ry is the Rydberg constant, ϵ_r the relative permittivity in GaAs, m_e the electron mass and r_s a dimensionless function of the z-coordinate given by

$$r_s^{-3}(z) = \frac{4\pi}{3}(\frac{r_o \epsilon_r m_e}{m^*})^3 n_{el}(z) \tag{2.20}$$

with $r_o = 5.29177\ 10^{-11}$ m. The Hartree potential follows from the Poisson equation

$$\tfrac{d^2}{dz^2} U_C(z) = \frac{e}{\epsilon_o \epsilon_r}\rho(z) = \frac{e^2}{\epsilon_o \epsilon_r}(\ n_{Don}(z) - n_{Acc}(z) - n_{el}(z)\ ) \tag{2.21}$$

where ϵ_o is the permittivity of vacuum and $\rho(z)$ is the space charge distribution. In equilibrium the charge distribution differs from zero since after the junction a charge redistribution takes place to elevate the discrepancies in the chemical potential in the different parts of the structure. The boundary conditions for the Poisson equation are:

$$\frac{d}{dz}U(z)\Bigg|_{\pm d_{Acc}} = 0; \qquad U(\ \pm d_{Acc}) = E_f + E_g - E_{Acc}/2$$

These conditions must always be satisfied and restrict the combinations of the parameters N_a and d_{Acc}. Globally their dependence can be given by

$$d_{Acc} = B + \sqrt{\frac{2E_g \epsilon_o \epsilon_r}{e^2 N_a}} \tag{2.22}$$

where B is the electron penetration depth$^{(13)}$. At non zero temperatures the electron charge density $n_{el}(z)$ is given by

$$n_{el}(z) = \sum_{i=0}^{\infty} \phi_i(z)\ \phi_i^{\dagger}(z) \int_{E_i}^{\infty} f(E, T, E_f) DOS_2(E)\, dE \tag{2.23}$$

where $\int_{-\infty}^{\infty} \phi_i(z)\ \phi_i^{\dagger}(z) dz = 1$. For low enough temperatures, $kT \ll E_i$, this leads to

$$n_{el}(z) = \sum_{i=0}^{Nbound-1} \phi_i(z)\ \phi_i^{\dagger}(z) \int_{E_i}^{E_f} DOS_2(E)\, dE \tag{2.24}$$

The summation index runs over all bound states i.e. $E_i < E_f$. The acceptor distribution function $n_{Acc}(z)$ looks like

$$N_{Acc}(z) = \begin{cases} N_a & \text{for } |z| < d_{Acc} \\ 0 & \text{else} \end{cases} \tag{2.25}$$

The precise shape of the donor distribution function $n_{Don}(z)$ can not be defined since it depends critically on MBE growth-parameters like the growth temperature$^{(14)}$ T_{growth}. For the time being we assume a rectangular function given by

$$N_{Don}(z) = \begin{cases} N_d & \text{for } |z| < \frac{1}{2}d_{Don} \\ 0 & \text{else} \end{cases} \tag{2.26}$$

The influence of the donor distribution shape has also been investigated.

Charge conservation states:

$$\int_{-\infty}^{\infty} \rho(z)dz = \frac{e^2}{\epsilon_o \epsilon_r} \int_{-\infty}^{\infty} (\ n_{Don}(z) - n_{Acc}(z) - n_{el}(z)\ )\ dz = 0 \tag{2.27}$$

So areal charge neutrality implies that the number of ionized donors N_{Don}^{+} equals the number of electrons in the 2-D electron gas N_{2DEG} plus the number of charged acceptors N_{Depl}^{-} with areal densities

$$N_{2DEG} = \int_{-\infty}^{\infty} n_{el}(z)\, dz \tag{2.28}$$

$$N_{Depl}^{-} = \int_{-\infty}^{\infty} n_{Acc}(z)\, dz = 2N_a d_{Acc} \tag{2.29}$$

$$N_{Don}^{+} = \int_{-\infty}^{\infty} n_{Don}(z)\, dz = N_d d_{Don} \tag{2.30}$$

Choosing the areal electron density N_{2DEG} as a system parameter seems self-evident. It directly gives the total number of bound states $Nbound$ and the Fermi energy E_f for a given set of eigen functions $\phi_i(z)$ and energy eigen values E_i . This follows from the relation

$$N_{2DEG} = \sum_{i=0}^{Nbound-1} \int_{E_i}^{E_f} DOS_2(E)\, dE \tag{2.31}$$

Once the areal electron density N_{2DEG} of a system is known the donor density N_d in equation 2-25 can be replaced by $\frac{N_{2DEG}+2N_a d_{Acc}}{d_{Don}}$.

The potential function $U(z)$ depends on the areal electron density $n_{el}(z)$ via the equations 2-20 and 2-21. This density function $n_{el}(z)$ however depends indirectly on the potential function via the eigen functions $\phi_i(z)$. Hence the set of equations defining the system must be solved self-consistently. The numerical method used to find self-consistent solutions will be discussed in the next subsection.

SUMMARY

A theoretical description of the system can be found if the following set of equations is solved self-consistently:

$$\left(-\frac{\hbar^2}{2m^*}\frac{d^2}{dz^2} + U(z) - E_n\right)\phi_n(z) = 0 \tag{2.32}$$

The potential $U(z)$ consists of two parts: a term $U_X(z)$ given by equation 2-19 and a Hartree term given by

$$\frac{d^2}{dz^2}U_C(z) = \frac{e^2}{\epsilon_o\epsilon_r}\left(n_{Don}(z) - n_{Acc}(z) - n_{el}(z) \right) \tag{2.33}$$

It turns out that our system is totally defined when the following parameters are defined: effective mass m^*, the the areal electron density N_{2DEG}; the energy band gap E_g; the bulk acceptor density N_a; the relative permittivity ϵ_r and finally the normalized donor distribution function $\tilde{n}_{Don}(z)$ defined as:

$$\tilde{n}_{Don}(z) = n_{Don}(z) \;/\; N^+_{Don} \tag{2.34}$$

In case this is a rectangular function this functional dependency can be expressed by one parameter only i.e. the donor spread distance d_{Don}. All other parameters and functions can be calculated from this set of parameters. This particular choice is not binding, however, careful thought should be paid to the selection of an other parameter set.

2.2 Numerical calculations and results

2.2.1 Iteration procedure

In order to find self-consistent solutions an iteration procedure is used; illustrated in figure 2.3. The idea of this iteration procedure is to calculate every iteration step a potential function $U^{(s)}(z)$ which in time will converge to the self-consistent potential $U(z)$. If one allows the potential function $U^{(s)}(z)$ in the iteration step s to change only slightly from the function $U^{(s-1)}(z)$ we have : $\lim_{s\to\infty} |U(z) - U^{(s)}(z)| = 0 \quad \forall\ z$. To start the iteration process it is necessary to have a first guess for the potential $U(z)$. We then solve the Schrödinger equation 2.32. With these eigen functions and eigen values the electron density $n_{el}(z)$ can be calculated from equation 2.24 and 2.31. Finally via the Poisson equation 2.21 and equation 2.19 a new potential $U_{new}(z)$ can be calculated. In order to ensure convergence the newly calculated potential $U_{new}(z)$ may only partially enter the Schrödinger equation of the next iteration step. We weighted this particular function by a factor θ ($0 \leq \theta \leq 1$). The potential $U^{(s)}(z)$ that enters the Schrödinger equation in the s^{th} iteration step is given by

$$U^{(s)}(z) = (1-\theta)\ U^{(s-1)}(z) + \theta\ U_{new}(z)$$

The iteration procedure is terminated after a desired accuracy in the potential function is reached. The number of iteration steps critically depends on the "quality" of the first guess (for the potential function). A "poor" first guess needs approximately 16 iteration steps. However when solving a number of different systems with only slightly different input parameters, the final potentials of these "nearby" systems produce very plausible first guesses.

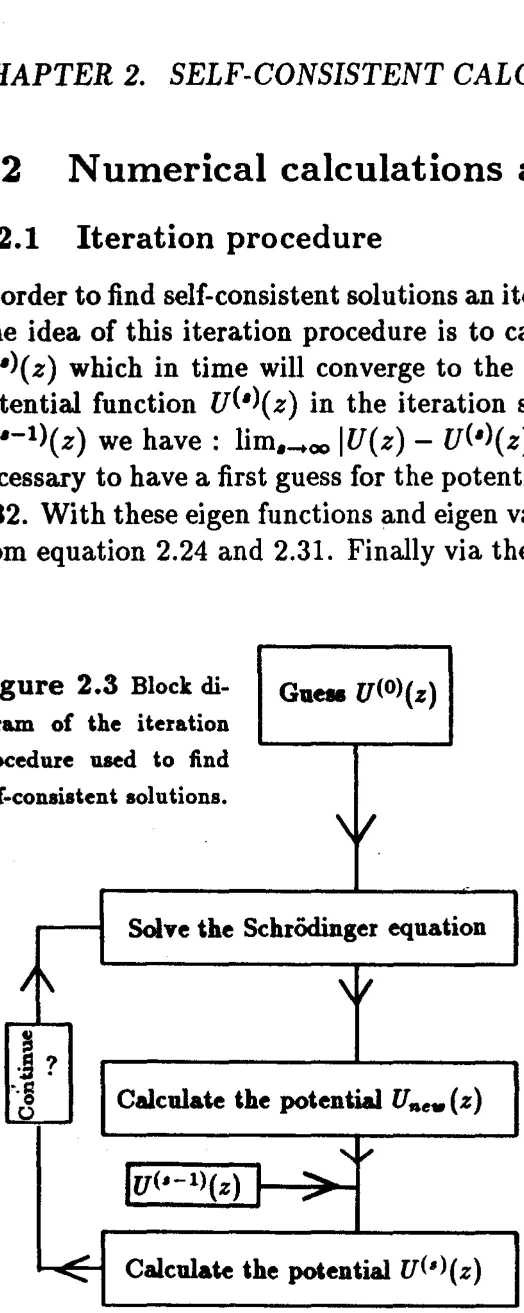

Figure 2.3 **Block diagram of the iteration procedure used to find self-consistent solutions.**

2.2.2 Solving the Schrödinger equation

The most difficult and time consuming part of an iteration step is the solution of the Schrödinger equation. A very suitable method for solving boundary value problems of non linear differential equations, like the Schrödinger equation, has only recently been developed and is called "multiple shooting"$^{(15)}$. This powerful method can solve an arbitrary set of n first order non-linear differential equations like: $\frac{d}{dt}\mathsf{y} = \mathsf{f}(t,\mathsf{y})$ on the interval $a \leq t \leq b$ with boundary values: $\mathsf{g}(\mathsf{y}(a),\mathsf{y}(b)) = \mathsf{0}$. The Schrödinger equation can be written as a set of four differential equations (equation 2.5) with appropriate boundary values. These equations can be rewritten to a set of differential equations of dimensionless quantities only:

$$\frac{d}{d\xi}\begin{pmatrix}\phi_n(\xi)\\ \psi_n(\xi)\\ \mu_n\\ N(\xi)\end{pmatrix} = \begin{pmatrix}\psi_n(\xi)\\ \frac{m^*}{m_{el}}R(U(\xi)-\mu_n)\cdot\phi_n(\xi)\\ 0\\ \phi_n(\xi)\phi_n(\xi)\end{pmatrix} \tag{2.35}$$

with $\xi = z/z_0, \phi_n(\xi) = \phi_n(z/z_0)/\sqrt{z_0}, \psi_n(\xi) = \psi_n(z/z_0)/\sqrt{z_0}, \mu_n = E_n/\mathcal{E}, U(\xi) = U(z/z_0)/\mathcal{E}$ and $R = \frac{2m_{el}\mathcal{E}z_0^2}{\hbar^2}$ where $z_0 = 100$ Å and $\mathcal{E} = 1\ meV$. In case the system is symmetric in the $z = 0$ plane one "only" has to solve the set of differential equations on the interval $z \geq 0$ with different boundary values for even and odd solutions. The infinite z-domain is truncated to a finite interval $[0,b]$ with $b = 500$ Å . The even solutions have boundary values: $N(0) = 0, \quad N(b) = \frac{1}{2}, \quad \phi_{2n}(b) = 0$ and $\psi_{2n}(0) = 0$ the odd solutions have boundary values: $N(0) = 0, \quad N(b) = \frac{1}{2}, \quad \phi_{2n-1}(0) = 0$ and $\psi_{2n-1}(b) = 0$. Clearly all even respectively odd solutions have the same boundary values whereas still all the different eigen functions of the Schrödinger equation can be calculated. This might seem a bit strange but it works well because one must give, besides the boundary values, a first guess for the four functions, ψ_n, ϕ_n, N and μ_n on the interval $[0,b]$. If these four input functions are close enough to the exact solutions the program will use the input functions to converge via some sort of Newton iteration process to the exact solutions within a given accuracy. For additional information about this method we refer to the book "Numerical solutions of boundary value problems for ordinary differential equations"(15).

2.2.3 Results

In this section we present a selected part of the calculations to give an impression of how various parameters influence the δ-dope system. As stated in section 2.1.3 a system is totaly defined by six parameters only namely: the effective mass m^*, the areal electron density N_{2DEG}, the energy band gap of GaAs E_g, the acceptor background concentration N_a, the relative permittivity of GaAs ϵ_r and the donor spread distance d_{Don}. In all our calculations we used the following quantities: $E_g = 1520\ meV$, $\epsilon_r = 12.0$ and $m^* = 0.067m_{el}$. The influence of the other three parameters, treated as system variables, has been investigated.

Influence of the areal electron density and the donor spread distance

The potential function $U(z)$ of a δ-dope has a sharp dip near the plane of Si-dopend as can be seen in figure 2.4a and 2.4b. These figures show the potential function for two different donor spread values together with the square of the envelope functions. The envelope functions are expressed in arbitrary units and superimposed on their corresponding lowest subband energy incase non parabolicity and exchange and correlation effects are included. The regions the donors are confined to are also displayed in these figures. The most interesting parameters of a δ-dope are: the areal electron density per subband n_i, the relative areal electron density per subband n_i/N_{2DEG}, the position of the subband energy above the conduction band $E_i - U(0)$ (in the manual refered to as E_i) and finally the position of the subband energy beneath the Fermi level $E_f - E_i$. All these parameters are tabulated and depicted in the additional manual(10) for different values of N_{2DEG} in the range $10^{12}/cm^2$ to $10^{13}/cm^2$ and various values of d_{Don} with 10 Å$\leq d_{Don} \leq$ 200 Å. For all these calculations the background acceptor concentration N_a was 10^{14} / cm^3. Figure 2.5 displays the dependency of the parameter n_i on the areal electron density N_{2DEG} for a donor spread distance of 40 Å.

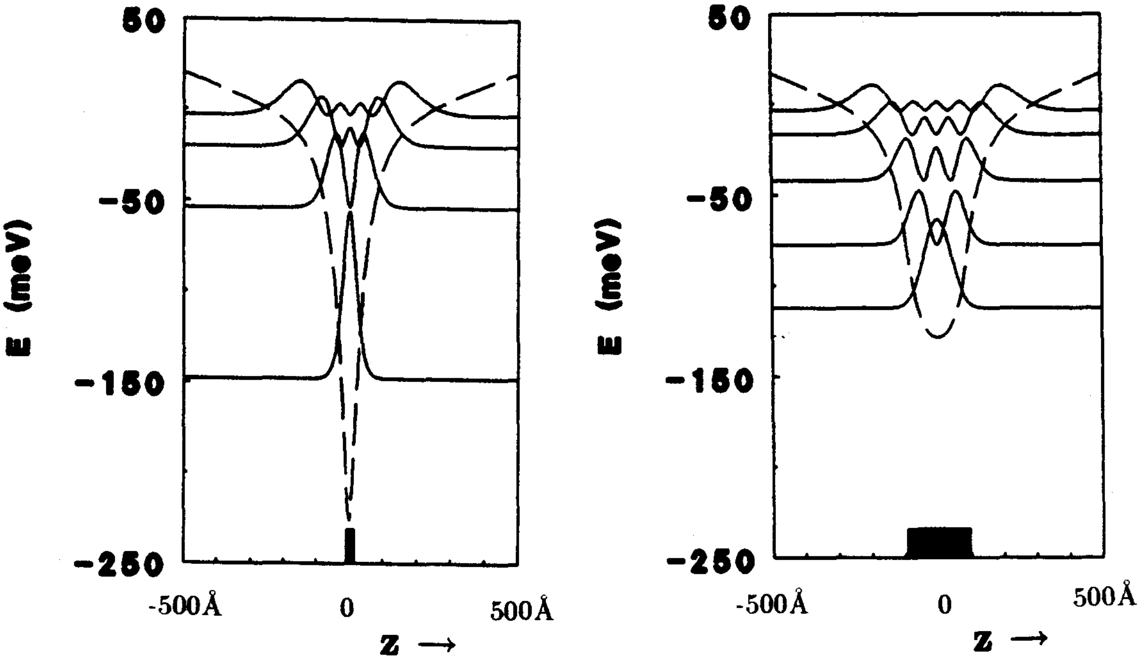

Figure 2.4a&b Results of self-consistent calculation of the potential function $U(z)$ incase the Fermi level E_f is set to zero for two different values of the donor spread distance. Figure a) d_{Don} = 20 Å and $N_{2DEG} = 8\ 10^{12}/cm^2$. Figure b) d_{Don} = 180 Å and $N_{2DEG} = 8\ 10^{12}/cm^2$.

Figure 2.5 Results of self-consistent calculation of the parameter n_i for a d_{Don} value of 40 Å.

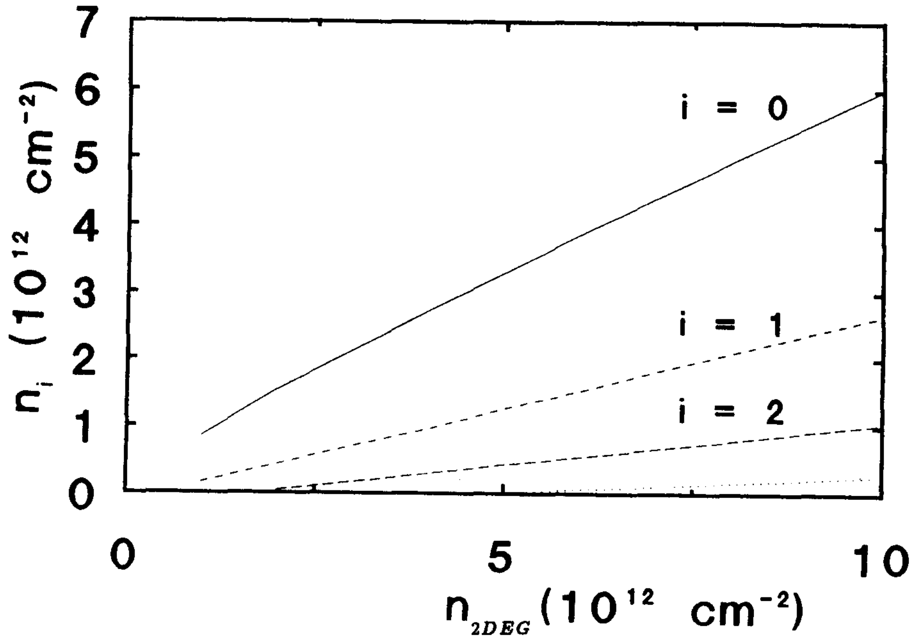

An interesting result is the linear dependency of n_i for small values of d_{Don}. For bigger donor spread distances this linearity is lifted. This conclusion follows even more directly when examening the dependency of the relative areal electron density per subband and N_{2DEG}. Figure 2.6 visualizes the influence of the donor spread distance on the parameter n_i for a constant areal elctron density of 8 $10^{12}/cm^2$.

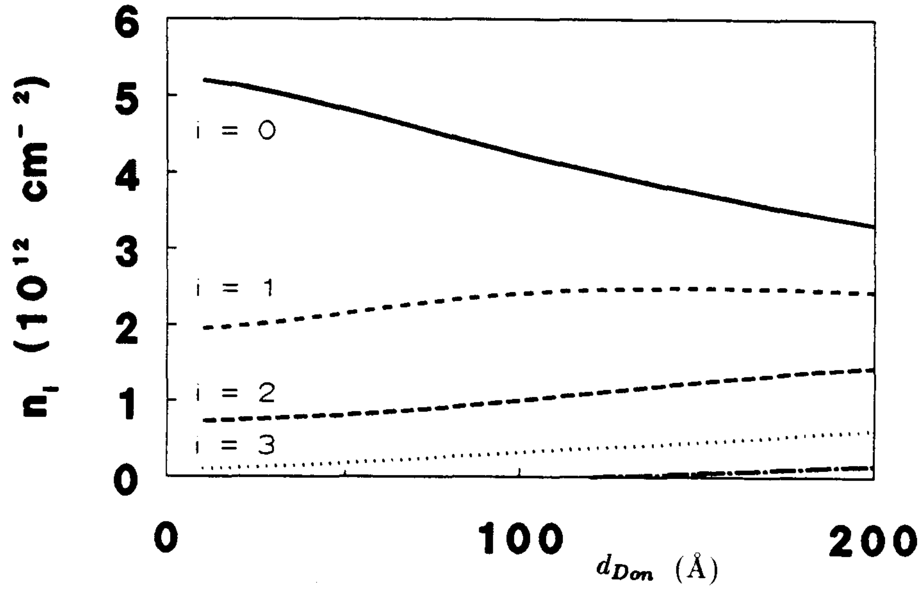

Figure 2.6 Results of self-consistent calculation of the parameter n_i for various d_{Don} values with a constant N_{2DEG} value of 8 $10^{12}/cm^2$.

This is an interesting figure since in principle one deduces for a given set of n_i values the best fitting d_{Don} value to that particular set. Note however the difficulty in deducing a reliable donor spread value for $d_{Don} \leq 40$ Å since the different subband electron densities do not differ much in this region.

Influence of acceptor concentration

To investigate the influence of the back ground acceptor concentration N_a we varied this particular system parameter over nearly four decades while keeping all other system parameters constant. The results of these calculations are visualized in figure 2.7. An important conclusion drawn from this figure is the fact that a δ-doped system is not heavily influenced by the acceptor concentration. This in contrast to an $Al_xGa_{(1-x)}As/GaAs$ heterostructure$^{(26)}$.

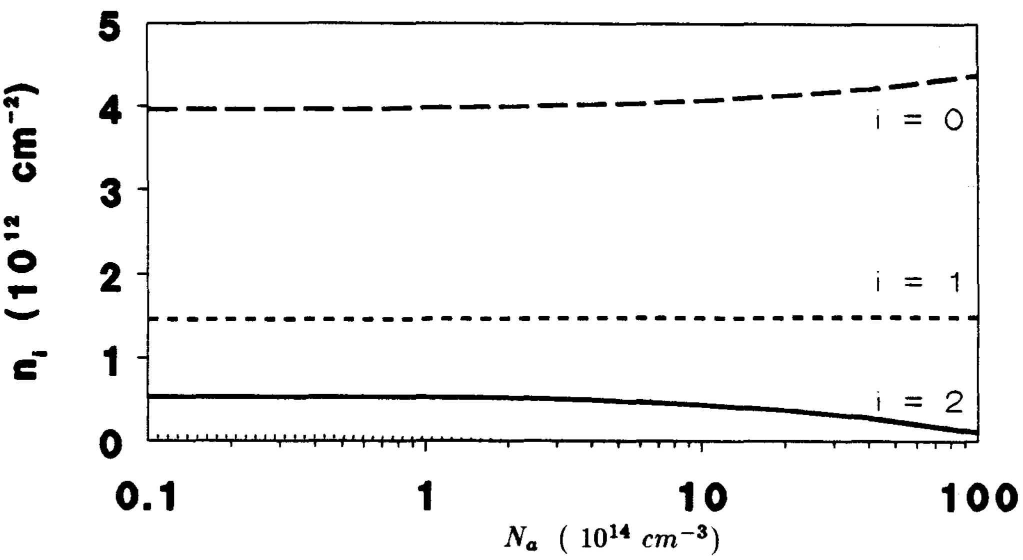

Figure 2.7 Results of self-consistent calculation of the parameter n_i for different acceptor concentration. The system parameters are: $N_{2DBG} = 6\ 10^{12}/cm^2$ and $d_{Don} = 20$ Å.

Influence of the donor distribution function shape

Most of the calculations were performed using a rectangular donor distribution function given by:

$$n_{Don}(z) = \begin{cases} \frac{N_{2DBG}+2d_{Acc}N_a}{d_{Don}} & \text{if } |z| < \frac{1}{2}d_{Don} \\ 0 & \text{else} \end{cases}$$

This particular choice for the shape of the donor distribution functions may be critized since it lacks back up of physical arguments. For instance, it seems more realistic to work with a function that falls off to zero more gradually on both sides. Or, when looking at the preperation procedure of the samples, why working with a symmetrical distribution function? The growth of δ-dopes with M.B.E can be described as a stop and go procedure during which hot silicon atoms ($T_{Si} \approx 1400\ ^{o}C$) are deposited on the relatively cold ($T_{growth} \approx 600\ ^{o}C$) GaAs wafer. Segregation, causing an asymetric donor distribution, and diffusion effects, causing a gradually and more wide spread distribution function, might be important processes; however neglected here. The influece of diffusion on δ-doped samples can be investigated via annealation$^{(16)}$.

$E_i - U(0)$	n_i	n_i/N_{2DEG}	$E_f - E_i$
32.2410	4.2505	0.5313	132.1200
92.9890	2.4155	0.3019	71.3730
135.3100	1.0090	0.1261	29.0520
155.0700	0.3249	0.0406	9.2918

$E_i - U(0)$	n_i	n_i/N_{2DEG}	$E_f - E_i$
37.3380	4.2526	0.5316	131.3200
99.5530	2.3531	0.2941	69.1090
138.4500	1.0539	0.1317	30.2120
158.9800	0.3404	0.0426	9.6820

Table 2.1a&b **Listing of system parameters to show the influence of the shape of the donor distribution function. Lefthand table (a) displays the results for a blok-function with parameters: $N_{2DEG} = 8\ 10^{12}/cm^2$ and $d_{Don} = 100$ Å. The righthand table (b) displays the results of a Gaussian donor distribution function with $\sigma = \frac{\sqrt{\pi}}{4} d_{Don}$ and $N_{2DEG} = 8\ 10^{12}/cm^2$.**

To investigate the influence of a donor distribution function that falls of more gradually to zero we used a Gaussian function given by:

$$n_{Don}(z) = \frac{N_{2DEG}+2d_{Acc}N_a}{\sqrt{\pi}\,\sigma}\, e^{-(z/\sigma)^2}$$

It is possible to minimize the discrepancies between system parameters like $E_i - U(0)$, n_i, n_i/N_{2DEG} and $E_f - E_i$ of a Gaussian and a rectangular distribution function. The relation between σ and d_{Don} for minimal parameter differences reads: $\sigma = \frac{\sqrt{\pi}}{4} d_{Don}$. Table 2.1a&b show the results for this optimal substitution of σ. Note the small differences between the parameters n_i, n_i/N_{2DEG} and $E_f - E_i$ whilst the discrepancies in $E_i - U(0)$ are no longer negligibly small. So differences in the donor distribution function shape are best seen in the quantity $E_i - U(0)$. This however is a difficult accessible quantity (optically?). Conclusively we state that the exact shape of the donor distribution function is not an accessible quantity when measuring system parameters like n_i, n_i/N_{2DEG} or $E_f - E_i$ (measuring quantities). The only information obtainable from measurements seems a mean donor spread distance d_{Don} or σ. Further investigations are necessary to see whether all kinds of distribution functions (especially the asymetric destribution functions are interesting) can be mapped on a system discribed by a rectangular distribution function.

Influence of exchange and correlation effects

In order to express somehow the exchange and correlation effects in an electron gas, one often uses the L.D.F.[4] formalism. Now all exchange and correlation effects of an electron gas can be incorporated by a potential U_X that is a function of the electron density only. We use the equation derived by Gunnarson and Lundqvist$^{(12)}$. This potential function is negative and for a δ-doped system it gradually falls of to zero for large values of $|z|$. The influence

---

[4] **Local Density Functional**

on system parameters like n_i, n_i/N_{2DEG} and $E_f - E_i$ is relatively small as can be seen from tables 2.4 a & b. The parameters $E_i - U(0)$ are mostly influenced and can differ a few meV's. Most changes of these parameters can also be found (to first order) via simple firts order perturbation theory.

$E_i - U(0)$	n_i	n_i/N_{2DEG}	$E_f - E_i$
32.2410	4.2505	0.5313	132.1200
92.9890	2.4155	0.3019	71.3730
135.3100	1.0090	0.1261	29.0520
155.0700	0.3249	0.0406	9.2918

$E_i - U(0)$	n_i	n_i/N_{2DEG}	$E_f - E_i$
31.892	4.1842	0.52303	130.30
91.592	2.3826	0.29783	70.596
132.57	1.0248	0.12810	29.618
151.42	0.3749	0.04686	10.768
161.23	0.0334	0.00418	0.9576

Table 2.2a&b Listing of system parameters to show the influence of exchange and correlation effects. Lefthand table (a) displays the results for a rectangular donor distribution function with parameters: $N_{2DEG} = 8\ 10^{12}/cm^2$ and $d_{Don} = 100$ Å in case exchange and correlation effects are included. The righthand table (b) displays the results when neglecting exchange and correlation effects.

We conclude that most system parameters are not heavily influenced when including an exchange and correlation potential like (2.19) and that the differences in system parameters are of the same magnitude as the effect of a different of the donor distribution shape.

Parabolicity versus non-parabolicity

Following Zrenner's strategy, non-parabolicity enters the self-consistent calculations only via the density of states function $DOS_2(E)$ (see appendix B). The non-parabolic density of states function can accommodate more electron states per energy interval than its parabolic analogue. For energies larger than $100meV$ these density of states functions can differ one another up to a factor 3/2. Tables 2.3 a & b display the calculated system parameters for a parabolic and a non-parabolic system. Comparing these two tables, shows that there are rather large differences between all parameters. This indicates that non-parabolicity may not be neglected.

$E_i - U(0)$	n_i	n_i/N_{2DEG}	$E_f - E_i$
32.2410	4.2505	0.5313	132.1200
92.9890	2.4155	0.3019	71.3730
135.3100	1.0090	0.1261	29.0520
155.0700	0.3249	0.0406	9.2918

$E_i - U(0)$	n_i	n_i/N_{2DEG}	$E_f - E_i$
32.979	4.0771	0.50964	145.68
95.407	2.3299	0.29124	83.249
140.36	1.0718	0.13398	38.296
163.01	0.4378	0.05473	15.646
175.68	0.0832	0.01041	2.9760

Table 2.3a&b Listing of system parameters to show the influence of non-parabolicity. Lefthand table (a) displays the results for a rectangular function with parameters: $N_{2DEG} = 8\ 10^{12}/cm^2$ and $d_{Don} = 100$ Å in case non-parabolicity is included. The righthand table (b) displays the results in case the parabolic dispersion relation is used for the self-consistent calculations.

Figure 2.8 displays the parameters $E_f - E_i$ versus the areal electron density. Note that for smaller values of the areal densities N_{2DEG} the system parameters are less influenced since for small N_{2DEG} values the two density of states functions become almost equivalent. On the other hand the bigger the areal density, the bigger the differences of system parameters will be. This latter conclusion is also valid for other system parameters like n_i, n_i/N_{2DEG} and $E_i - U(0)$.
Conclusion: non-parabolicity must be included in the self-consistent calculations especially for areal electron densities above 1 $10^{12}/cm^2$.

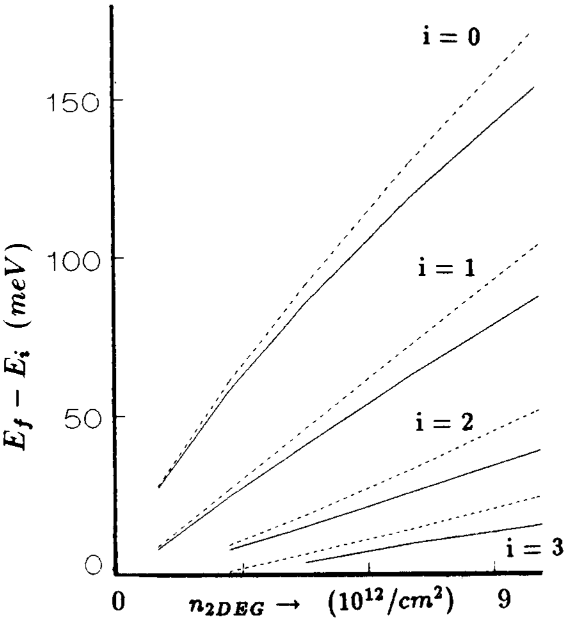

Figure 2.8 The parameters $E_f - E_i$ versus the arael electron density N_{2DEG} are displayed for the parabolic (- -) and the non-parabolic (—) dispersion relation.

Chapter 3

Signal analysis

3.1 Introduction

In a magnetic field the density of states DOS acquires an oscillatory component ΔDOS which, at low fields, can be written as(17)

$$\frac{\Delta DOS(E,T,B)}{DOS_0} = 2\sum_{r=1}^{\infty} D(rx) \cdot e^{\frac{-r\pi}{\omega_c \tau_s}} \cos(\frac{2r\pi E}{\hbar\omega_c} - r\pi) \tag{3.1}$$

where DOS_0 is the zero-field density of states, ω_c is the cyclotron frequency and E is the electron energy. The function $D(x)$ is defined as

$$D(x) = \frac{x}{\sinh(x)} \tag{3.2}$$

with $x = 2\pi^2 k_B T/\hbar\omega_c$. This function incorporates the temperature dependence of equation (3.1). The single particle life time τ_s is related to the broadened (Lorentzian) Landau levels width Γ such that $\Gamma = \hbar/2\tau_s$. Isihara and Smrčka(17) have shown that these oscillations in the density of states give rise to oscillatory components in all other physical properties. Especially in the conductivity σ that can be written as:

$$\sigma_{xx} = \frac{e}{B}\frac{N_{eff}}{1+\omega_c^2\tau^2}\omega_c\tau \tag{3.3}$$

$$\sigma_{xy} = e\frac{\partial N}{\partial B} - \omega_c\tau\sigma_{xx} \tag{3.4}$$

where N_{eff} is the effective number of electrons participating in the electrical transport and N is the number of states below the Fermi energy. At zero magnetic field equation (3.3) results in $\sigma_{xx} = N_0\tau_t e^2/m^*$ and thus the τ used in our expressions for the conductivity is in fact the magnetic field-dependent transport life time τ_t.

The difference between the single-particle life time τ_s (also refered to as quantum life time) and the transport scattering time τ_t is that the latter is weighted by the scattering angle θ, i.e.

$$\frac{1}{\tau_s} = \int \nu(\theta)d\Omega \tag{3.5}$$

$$\frac{1}{\tau_t} = \int (1-\cos(\theta)) \cdot \nu(\theta)d\Omega \tag{3.6}$$

The scattering time τ_t is related to the conductivity σ by

$$\sigma = \frac{n\, e^2 \tau_t}{m^*} = n\; e\; \mu \tag{3.7}$$

In high-mobility GaAs heterojunctions the ratio of τ_t and τ_s can be relatively large$^{(18)}$ (≥ 10). In that situation the single-particle relaxation time τ_s cannot be estimated from the mobility measurements. In δ-doped GaAs samples however, the different subband mobilities μ_i are usually small compared to that of a heterojunction, because of a larger overlap between the subband envelope-functions and the random distributed Coulomb scattering centers. This would imply that $\tau_t/\tau_s \approx 1$ $^{(17)}$.

The oscillatory parts in the conductivity N_{eff} and $1/\tau_t$, are proportional to the density of states at the Fermi energy E_F.

$$N_{eff} = N_0\,(1 + \frac{\Delta DOS(E_F)}{DOS_0}) \tag{3.8}$$

$$\frac{1}{\tau_t} = \frac{1}{\tau_0}(1 + \frac{\Delta DOS(E_F)}{DOS_0}) \tag{3.9}$$

When $E_F \gg \hbar/\tau_t$ and $E_F \gg \hbar\omega_c$ (both conditions are usually satisfied) we may write$^{(17)}$:

$$\frac{\partial N}{\partial B} = \frac{N_0}{B} \cdot \frac{\Delta DOS(E_F)}{DOS_0} \tag{3.10}$$

Using these relations and keeping only the terms linear in $\frac{\Delta DOS(E_F)}{DOS_0}$ finally results in

$$\sigma_{xx} = \frac{\sigma_0}{1+\omega_c^2\tau_0^2}(1 + \frac{2\omega_c^2\tau_0^2}{1+\omega_c^2\tau_0^2}\frac{\Delta DOS(E_F)}{DOS_0}) \tag{3.11}$$

$$\sigma_{xy} = -\frac{\sigma_0\omega_c\tau_0}{1+\omega_c^2\tau_0^2}(1 - \frac{3\omega_c^2\tau_0^2+1}{\omega_c^2\tau_0^2(1+\omega_c^2\tau_0^2)}\frac{\Delta DOS(E_F)}{DOS_0}) \tag{3.12}$$

Here $\sigma_0 = \frac{e^2}{m^*}N_0\tau_0$ is the conductivity at zero magnetic field. The expressions 3.11 and 3.12 are useful when describing a 2-D electron gas with only one subband. A typical property of a δ-doped system is that more than one subband is occupied. When interactions between the subbands are neglected we have the following expression for σ_{xx} and σ_{xy} in a multi-subband system since conductivity is an additive quantity

$$\sigma_{xx} = \sum_{i=0}^{Nbound-1} \frac{\sigma_{0,i}}{1+\omega_c^2\tau_{0,i}^2}(1 + \frac{2\omega_c^2\tau_{0,i}^2}{1+\omega_c^2\tau_{0,i}^2}\frac{\Delta DOS(E_F-E_i)}{DOS_0}) \tag{3.13}$$

$$\sigma_{xy} = -\sum_{i=0}^{Nbound-1} \frac{\sigma_{0,i}\omega_c\tau_{0,i}}{1+\omega_c^2\tau_{0,i}^2}(1 - \frac{3\omega_c^2\tau_{0,i}^2+1}{\omega_c^2\tau_{0,i}^2(1+\omega_c^2\tau_{0,i}^2)}\frac{\Delta DOS(E_F-E_i)}{DOS_0}) \tag{3.14}$$

where $\sigma_{0,i} = \frac{e^2}{m^*}N_{0,i}\tau_{0,i}$ is the conductivity at zero magnetic field in the i-th subband and E_i the ground state energy of the i-th subband. One can calculate ρ_{xx} and ρ_{xy} via the tensor relations

$$\rho_{xx} = \frac{\sigma_{xx}}{\sigma_{xx}^2 + \sigma_{xy}^2} \tag{3.15}$$

$$\rho_{xy} = -\frac{\sigma_{xy}}{\sigma_{xx}^2 + \sigma_{xy}^2} \tag{3.16}$$

This leads to rather simple expressions for the resistivity ρ in a one subbband system assuming that $\frac{\Delta DOS(E_F)}{DOS_0}$ is small

$$\rho_{xx} = \rho_0(1 + 2\frac{\Delta DOS(E_F)}{DOS_0}) \tag{3.17}$$

$$\rho_{xy} = \rho_0\omega_c\tau_0(1 - \frac{1}{\omega_c^2\tau_0^2}\frac{\Delta DOS(E_F)}{DOS_0}) \tag{3.18}$$

A multi-subband system, like δ-doped GaAs, has very complex expressions for the longitudinal and Hall resistivities. This will be worked out in more detail in the next section.

3.2 Magnetic field modulation

When a small time dependent magnetic field $B_{mod}(t)$ is superimposed on a quasi static magnetic field B the resistivity will change only slightly under the condition $B_{mod}(t) \ll$ B. Choosing the modulation field like $B_{mod}(t) = B_m \sin(\Omega t)$ suggests the use of Lock-in techniques to accurately resolve the oscillatory parts of the signal i.e. the Ωt and $2\Omega t$ components of the signal. This technique is very powerful and especially useful when studying small changes in magnetic field dependent signals like SdH-oscillations. The conductivity in a magnetic field of a multi-subband system can be described by the expressions 3.13 and 3.14. One can derive from these formulas the following expressions to first order in $\frac{\Delta DOS(E_F-E_i)}{DOS_0}$ for the resistivity in a multi-subband system:

$$\rho_{xx} = \frac{A}{A^2+C^2}(\ 1\ +\ \sum_{i=0}^{Nbound-1} \xi_i\frac{(C^2-A^2)\,b_i + 2CA\,d_i}{A(A^2+C^2)}\ ) \tag{3.19}$$

$$\rho_{xy} = \frac{C}{A^2+C^2}(\ 1\ +\ \sum_{i=0}^{Nbound-1} \xi_i\frac{-2CA\,b_i + (C^2-A^2)\,d_i}{C(A^2+C^2)}\ ) \tag{3.20}$$

where

$$A = \sum_{i=0}^{Nbound-1} \frac{\sigma_{0,i}}{1+\omega_c^2\tau_{0,i}^2} \tag{3.21}$$

$$C = \sum_{i=0}^{Nbound-1} \frac{\sigma_{0,i}\omega_c\tau_{0,i}}{1+\omega_c^2\tau_{0,i}^2} \tag{3.22}$$

$$b_i = \frac{2\sigma_{0,i}\omega_c^2\tau_{0,i}^2}{(1+\omega_c^2\tau_{0,i}^2)^2} \tag{3.23}$$

$$d_i = \sigma_{0,i}\omega_c\tau_{0,i}\cdot\frac{3\omega_c^2\tau_{0,i}^2+1}{\omega_c^2\tau_{0,i}^2(1+\omega_c^2\tau_{0,i}^2)^2} \tag{3.24}$$

$$\xi_i = \frac{\Delta DOS(E_F-E_i)}{DOS_0} = 2\sum_{r=1}^{\infty}(-1)^r D(rx)\cdot e^{\frac{-r\pi}{\omega_c\tau_s}}\cos(\frac{2r\pi}{P_iB}) \tag{3.25}$$

Choosing a magnetic field like $\tilde{B} = B + B_m \sin(\Omega t)$ will affect the function ξ_i like

$$\xi_i = \sum_{r=1}^{\infty} G_{r,i}(\tilde{B}) \cos(\frac{2\pi\ r}{P_i B(1 + \frac{B_m}{B} \sin(\Omega t))}) \tag{3.26}$$

where $G_{r,i}(B) = 2(-1)^r D(rx) e^{\frac{-r\pi}{\omega_c \tau_{s,i}}}$. The functions x and D have been defined in the former section. For $B_m \ll B$ this can be rewritten to

$$\xi_i = \sum_{r=1}^{\infty} G_{r,i}(\tilde{B}) \cos(\tfrac{2\pi r}{P_i B} - r\alpha \sin(\Omega t)) \tag{3.27}$$

where $\alpha = \frac{2\pi B_m}{P_i B^2}$. The functions $G_{r,i}, a_i, b_i, c_i, A, C$ and d_i are slowly varying in the magnetic field B; so one may neglect the oscillatory part of the magnetic field in these functions. This implies that the modulation field affects the resistivity most strongly via the function ξ_i. A Fourier series expansion of ξ_i gives:

$$\xi_i = \sum_{r=1}^{\infty} G_{r,i}(B) \cos(\tfrac{2\pi r}{P_i B} - r\alpha \sin(\Omega t)) \tag{3.28}$$

$$= \sum_{r=1}^{\infty} G_{r,i}(B) \left\{ \ \cos(\tfrac{2\pi r}{P_i B}) \cos(\ r\alpha \sin(\Omega t)\ ) \ + \ \sin(\tfrac{2\pi r}{P_i B}) \sin(\ r\alpha \sin(\Omega t)\ ) \ \right\}$$

$$\begin{aligned} = \sum_{r=1}^{\infty} G_{r,i}(B) \ \Big\{ \ & \cos(\tfrac{2\pi r}{P_i B}) \left[J_0(r\alpha) + 2 \sum_{n=1}^{\infty} J_{2n}(r\alpha) \cos(2n\Omega t) \right] \\ + \ & \sin(\tfrac{2\pi r}{P_i B}) \left[2 \sum_{n=0}^{\infty} J_{2n+1}(r\alpha) \sin(\ (2n+1)\Omega t) \right] \ \Big\} \end{aligned}$$

Here we use the possibility of writing the functions $\cos(z \sin(x))$ and $\sin(z \sin(x))$ as a infinite series of Bessel-functions i.e.:

$$\cos(\ z \sin(x)\ ) = J_0(z) + 2 \sum_{n=1}^{\infty} J_{2n}(z) \sin(2nx)$$

$$\sin(\ z \sin(x)\ ) = 2 \sum_{n=0}^{\infty} J_{2n+1}(z) \sin(\ (2n+1)x)$$

Detection of the first (Ω) harmonic component in the resistivities finally gives:

$$\rho_{xx_\Omega} = 2 \sum_{i=0}^{Nbound-1} \frac{(C^2 - A^2)\, b_i + 2CA\, d_i}{(A^2 + C^2)^2} \sum_{r=1}^{\infty} J_1(\tfrac{2\pi r B_m}{P_i B^2}) \sin(\tfrac{2\pi r}{P_i B})\, G_{r,i}(B) \tag{3.29}$$

$$\rho_{xy_\Omega} = 2 \sum_{i=0}^{Nbound-1} \frac{-2CA\, b_i + (C^2 + A^2)\, d_i}{(A^2 + C^2)^2} \sum_{r=1}^{\infty} J_1(\tfrac{2\pi r B_m}{P_i B^2}) \sin(\tfrac{2\pi r}{P_i B})\, G_{r,i}(B) \tag{3.30}$$

and for the second harmonic (2Ω) component

$$\rho_{xx_{2\Omega}} = 2 \sum_{i=0}^{Nbound-1} \frac{(C^2 - A^2)\, b_i + 2CA\, d_i}{(A^2 + C^2)^2} \sum_{r=1}^{\infty} J_2(\tfrac{2\pi r B_m}{P_i B^2}) \cos(\tfrac{2\pi r}{P_i B})\, G_{r,i}(B) \tag{3.31}$$

$$\rho_{xy_{2\Omega}} = 2\sum_{i=0}^{Nbound-1} \frac{-2CA\,b_i + (C^2 + A^2)\,d_i}{(A^2+C^2)^2} \sum_{r=1}^{\infty} J_2(\tfrac{2\pi r B_m}{P_i B^2})\cos(\tfrac{2\pi r}{P_i B})\,G_{r,i}(B) \tag{3.32}$$

Define the functions $\mathcal{G}_i^{Rmax}(B)$ and $\mathcal{H}_i^{Rmax}(B)$ as:

$$\mathcal{G}_i^{Rmax}(B) = \sum_{r=1}^{Rmax} J_1(\tfrac{2\pi r B_m}{P_i B^2})\sin(\tfrac{2\pi r}{P_i B})\,G_{r,i}(B)$$

$$\mathcal{H}_i^{Rmax}(B) = \sum_{r=1}^{Rmax} J_2(\tfrac{2\pi r B_m}{P_i B^2})\cos(\tfrac{2\pi r}{P_i B})\,G_{r,i}(B)$$

These functions are shown in figure 3.1 and 3.2 for two upper limits $Rmax$ of the summation index r. From these figures we conclude that, since the whole theory is based on a low field approximation, it is permitted to truncate the series after the first term. The final expressions for the first harmonic component in the longitudinal and Hall resistivity now read:

$$\rho_{xx_\Omega} = 2\sum_{i=0}^{Nbound-1} \frac{(C^2 - A^2)\,b_i + 2CA\,d_i}{(A^2+C^2)^2} J_1(\tfrac{2\pi B_m}{P_i B^2})\sin(\tfrac{2\pi}{P_i B})\,G_{1,i}(B) \tag{3.33}$$

$$\rho_{xy_\Omega} = 2\sum_{i=0}^{Nbound-1} \frac{-2CA\,b_i + (C^2 + A^2)\,d_i}{(A^2+C^2)^2} J_1(\tfrac{2\pi B_m}{P_i B^2})\sin(\tfrac{2\pi}{P_i B})\,G_{1,i}(B) \tag{3.34}$$

while the second harmonic (2Ω) components read

$$\rho_{xx_{2\Omega}} = 2\sum_{i=0}^{Nbound-1} \frac{(C^2 - A^2)\,b_i + 2CA\,d_i}{(A^2+C^2)^2} J_2(\tfrac{2\pi B_m}{P_i B^2})\cos(\tfrac{2\pi}{P_i B})\,G_{1,i}(B) \tag{3.35}$$

$$\rho_{xy_{2\Omega}} = 2\sum_{i=0}^{Nbound-1} \frac{-2CA\,b_i + (C^2 + A^2)\,d_i}{(A^2+C^2)^2} J_2(\tfrac{2\pi B_m}{P_i B^2})\cos(\tfrac{2\pi}{P_i B})\,G_{1,i}(B) \tag{3.36}$$

Figure 3.1 The function $\mathcal{G}_i^{Rmax}(B)$ for $Rmax = 1$ (straight) and $Rmax = 20$ (dotted). Used parameters: $\mu_s = 0.2\ m^2/Vs$; $P_0 = 0.0242\ 1/T$; $B_m = 30\ mT$.

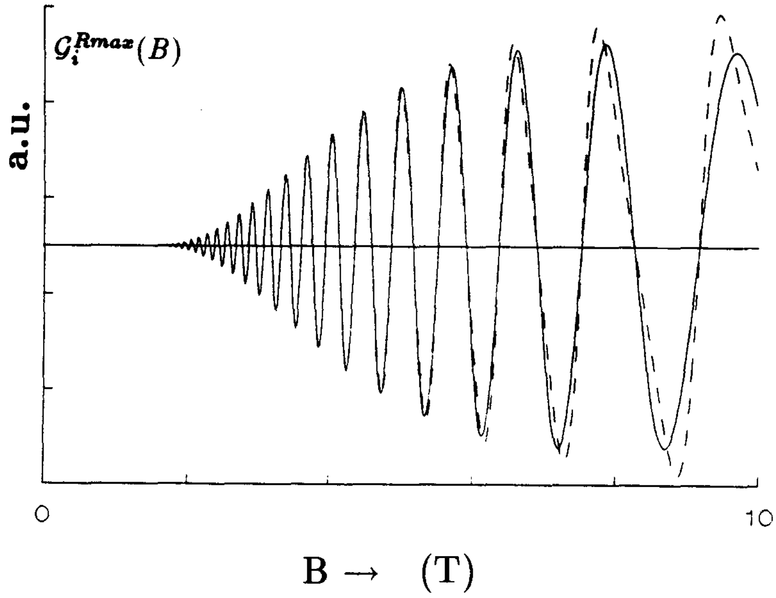

Figure 3.2 The function $\mathcal{H}_i^{Rmax}(B)$ for $Rmax = 1$ (straight) and $Rmax = 20$ (dotted). Same parameters as in figure 3.1.

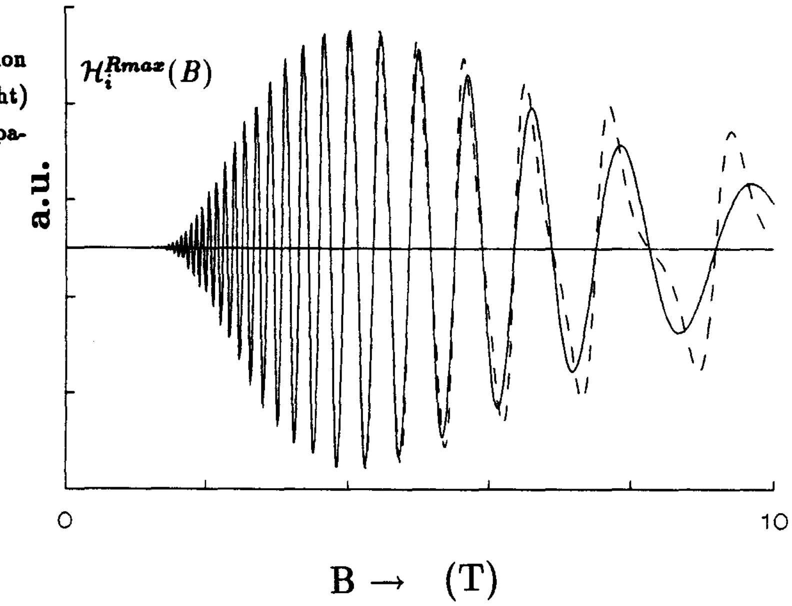

The essential part of the functions ρ_{Ω} and $\rho_{2\Omega}$ is the periodicity in the reciprocal magnetic field. Although the above expressions are derived for low magnetic fields one assumes, without further theoretical reasoning, that these formulas remain globaly valid for high field: this means that the resistivity remains periodic in 1/B with periodicity P_i. This periodicity P_i is related to the number of electrons in the subband i, n_i, via the relation

$$n_i = \frac{4.84\ 10^{-2}}{P_i}\ (10^{12}\ cm^{-2}) \tag{3.37}$$

Now n_i becomes an accessible quantity when magnetic field modulation techniques are used since in pricipal P_i can be extracted from (Fast) Fourier Transforms of the field modulated resistivity, i.e. ρ_{xx}, in the reciprocal magnetic field. Notice that not all the oscillating terms that contribute to the signal have the same weight function (amplitude). The subband with the highest mobility result in the major contribution to the signal. In δ-dopes the different subband mobilities[1], μ_i, can differ one another up to a factor $5^{(1)}$. The lowest subbands will contribute neglectably to the signal at low fields because of there relatively small mobility. This can be understood by examining the (weight)function $G_{r,i}(B)$. This (weight)function is exponentially dependend of the scattering mobility and becomes close to unity for B $\gg 1/\mu_{s,i}$ while it falls of rapidly to zero at lower fields. If one wants to resolve all the subbands then one should measure to fields up to $1/\mu_{s0}$. We characterized the δ-dopes by measuring with fields up to 20 Tesla. In this range of fields all the periods P_i could be resolved. The accuracy with which the periods can be resloved from the measurements will be discussed in the next section.

---

[1] No reliable values have yet been published or calculated!

3.3 Fourier transforms

3.3.1 Fourier and fast Fourier transform

Fourier transformations are especially useful when extracting periodic behaviour in arbitrary smooth functions. Simultaneous visualization of a function and its Fourier transform is often the way to overcome lacking insight in problems. The Fourier transform(19) of a function $f(x)$ is defined as

$$\int_{-\infty}^{\infty} f(x)e^{-i2\pi xs}dx \tag{3.38}$$

This integral, which is a function of s, may be written as $\mathcal{F}(s)$. The inverse Fourier transform is defined as

$$f(x) = \int_{-\infty}^{\infty} \mathcal{F}(s)e^{i2\pi xs}ds \tag{3.39}$$

Another way of writing the two successive transformations is

$$f(x) = \int_{-\infty}^{\infty} \left[\int_{-\infty}^{\infty} f(y)e^{-i2\pi ys}dy \right] e^{i2\pi xs}ds \tag{3.40}$$

also called Fourier's integral theorem. There are some restrictions under which these equations are valid. First the integral of $\mid f(x) \mid$ from $-\infty$ to ∞ should exist and secondly all discontinuities in $f(x)$ must be finite and replaced by their midvalue. Any function satisfying these conditions can be written as 3.40. Some authors lump the factor 2π with s to yield the following set of equations

$$\mathcal{F}(s) = \int_{-\infty}^{\infty} f(x)e^{-ixs}dx \tag{3.41}$$

$$f(x) = \frac{1}{2\pi} \int_{-\infty}^{\infty} \mathcal{F}(s)e^{ixs}ds \tag{3.42}$$

A third also often used definition of the Fourier transform is the symmetric version of the last two equations

$$\mathcal{F}(s) = \frac{1}{\sqrt{2\pi}} \int_{-\infty}^{\infty} f(x)e^{-ixs}dx \tag{3.43}$$

$$f(x) = \frac{1}{\sqrt{2\pi}} \int_{-\infty}^{\infty} \mathcal{F}(s)e^{ixs}ds \tag{3.44}$$

We will use the first version. In practice it's impossible to measure a quantity $f(x)$ with infinite resolution on an infinite x-domain. One usually has a finite set of data points $f(x_i)$ on a finite x-interval. The reduction of the x-domain $x \in R$ to an interval (x_{min}, x_{max}) makes the continuous s-domain $s \in R$ discrete $s \in \{l \cdot \Delta s \mid l \in Z\}$ when assuming $f(y + x_{max} - x_{min}) = f(y)$; where $\Delta s = 1/(x_{max} - x_{min})$. All frequencies in the Fourier spectrum are integer values of the minimal frequency Δs. Suppose we have measured a quantity $f(x)$ at equi-distant points $x \in \{x_{min} + k \cdot \Delta x \mid k \in (0, \cdots, N-1)\}$ with $\Delta x = 1/(N\Delta s)$. This set of data points can be written as

$$\sum_{k=0}^{N} f(x_k) \cdot \delta(k - \tfrac{(x - x_{min})}{\Delta x}) = \sum_{k=0}^{N} f(x) \cdot \delta(k - \tfrac{(x - x_{min})}{\Delta x}) \equiv f(x) \cdot D(x) \tag{3.45}$$

The information about $f(x)$ in between the intervals is not contained in the product; however, the values of $f(x)$ at the values $x = x_k$ are preserved.

The convolution of two functions f and g is another function h defined by the integral

$$h(x) = \int_{-\infty}^{\infty} f(u)\, g(x-u)\, du \equiv f(x) * g(x) \tag{3.46}$$

The function $h(x)$ is a linear function of $f(x)$ since it is a linear sum of values of $f(x)$, duly weighted as described by $g(x)$. The reason for introducing the convolution theorem is the fact that it's Fourier transform is the product of the Fourier transform of the two original functions.

$$f(x) * g(x) \overset{\mathcal{F.T}}{\Longrightarrow} \mathcal{F}(s)\, \mathcal{G}(s) \tag{3.47}$$

A similar relation holds for inverse Fourier transformations

$$f(x)\, g(x) \overset{\mathcal{F.T}}{\Longrightarrow} \mathcal{F}(s) * \mathcal{G}(s) \tag{3.48}$$

Generally we can say that the convolution of two functions means multiplication of their transforms. Applying the above theorem on a sampled function (which is in fact a product of a continuous function and a series of delta functions), enables us to predict the general form of its Fourier transform.

$$f(x)\, D(x) \overset{\mathcal{F.T}}{\Longrightarrow} \mathcal{F}(s) * \mathcal{D}(s) \tag{3.49}$$

The function $\mathcal{D}(s)$ can be written as a convolution of two functions, $\mathcal{III}(s)$ and $\mathcal{S}(s)$, since one can write $D(x)$ as a product of two more elementary functions

$$D(x) = H(x - x_{min}) \cdot H(x_{max} - x) \cdot III(\tfrac{(x-x_{min})}{\Delta x}) = S(x) \cdot III(\tfrac{(x-x_{min})}{\Delta x}) \tag{3.50}$$

where $H(x)$ is the Heaveside step function and $III(x)$ (pronounced as shah) is defined as

$$III(x) = \sum_{n=-\infty}^{\infty} \delta(x-n). \tag{3.51}$$

Graphically this is illustrated in figure 3.3. If $1/\Delta x$ is chosen too small compared to the width of the Fourier transform of a function f, serious problems arise. The convolution with the function $\mathcal{F}(s)$ results in the overlapping wave form illustrated in figure 3.4.

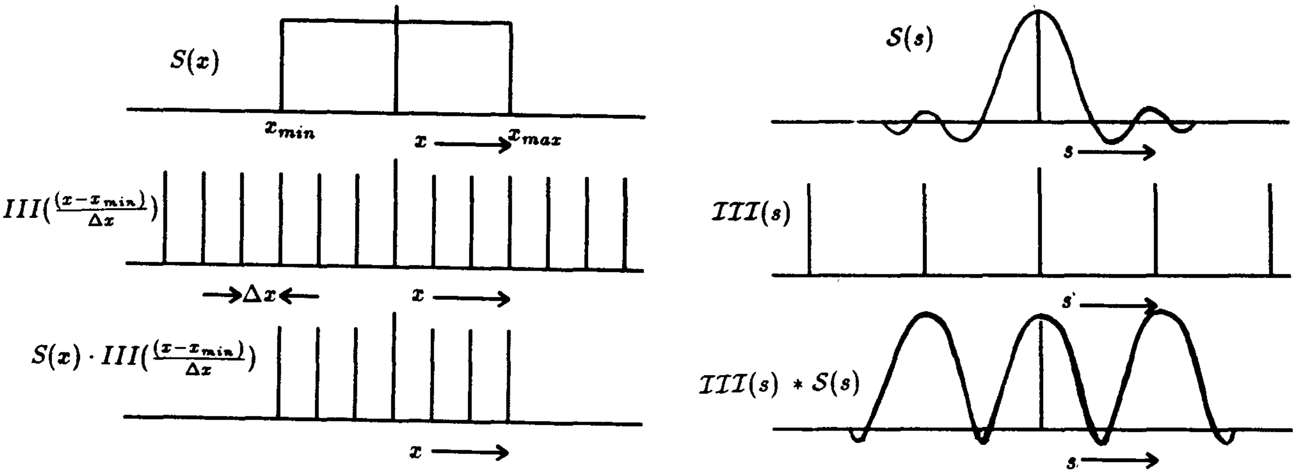

Figure 3.3 The product of two functions leads to a convolution of the transforms. This is illustrated for the product in the x-domain of the functions $III(x)$ and $S(x)$.

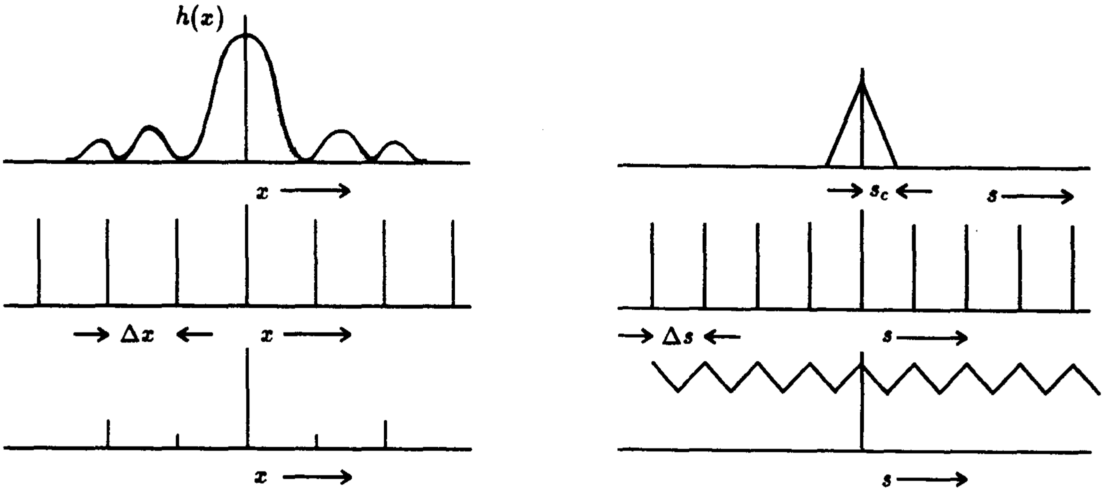

Figure 3.4 Example of too low sampling in the x-domain of a function $h(x)$. It is impossible to reconstruct the function $h(x)$ from it's sampled Fourier transform via a inverse Fourier transformation since the "triangles" overlap.

This distortion of the desired Fourier transform of a sampled function is known as aliasing. It's caused by a too low sample frequency $1/\Delta x$. To exclude aliasing the sample frequency must at least be two times s_c, where s_c is the highest frequency component of the Fourier transform of the continuous function $f(x)$. The fast Fourier transform is simply an algorithm that can compute the discrete Fourier transform much more rapidly than other available algorithms. We will not discuss the computational aspects of the algorithm but merely look at some applicatioms. The first step in applying the discrete transform is to choose the number of samples N (where ${}^2\log N$ is an integer value), a sample interval Δx and a minimal x value x_{min}. Note that the value of the function at a discontinuity must be defined to be the midvalue if the inverse Fourier transform is to hold. The discrete Fourier transform of our data array $f(x_k)$ now becomes a complex array $\mathcal{F}(s_n)$

$$\mathcal{F}(s_n) = \Delta x \cdot \sum_{k=0}^{N-1} f(x_{min} + k\Delta x)e^{-2\pi i n k/N} \qquad s_n = \frac{n}{N\Delta x} \tag{3.52}$$

The scale factor Δx is introduced to produce equivalance between the continuous and discrete transformations. The discrete transformations are symmetrical about $N/2$. This follows because the real part of the transformation is even and the results for $n > N/2$ are simply negative frequency results. It's recommendable to use the true frequency scale in the plots instead of the array index n. The relation between the index n and the true frequency reads

$$s_n = \begin{cases} \frac{n}{N\Delta x} & \text{for } 0 \leq n < N/2 \\ \frac{n-N}{N\Delta x} & \text{for } N/2 \leq n < N \end{cases} \tag{3.53}$$

The FFT results are spaced in frequency by the interval $\Delta s = 1/(N\Delta x)$. If a higher resolution is desired then an increase in N is preferable to an increase in Δx since this can cause aliasing. Beware that the term increase in resolution is ambiguous in that one is not sure if a larger or smaller resolving power is implied. A common mistake made by FFT users is to increase N by appending zero's to the sampled and truncated function and to interpret the results as having enhanced resolution. The frequency resolution has already been set and the convolution operation of adding zero's merely provides additional frequency samples by interpolating the original frequency results. Resolution is determined by the "time duration" of a signal which is set by the truncation interval. For periodic functions with known periods, one can choose $N\Delta x$ equal to an integer multiple of a period. Whenever it is impossible to choose N sufficiently large or where the periodic function is not known, the concept of a data-weighting function must be employed.

3.3.2 The data-weighting functions

The use of data-weighting functions can be a very powerful technique to minimize the undesired effects of a non-optimal x-domain truncation. In this section we will investigate the effect of the four most used weighting functions on the discrete frequency spectrum.

Rectangular weighting function

Truncating a function $f(x)$ in the x-domain can be seen as a multiplication of a rectangular weighting function $R(x)$ and the original function $f(x)$ where the width of the function $R(x)$ is $N\Delta x = (x_{max} - x_{min})$.

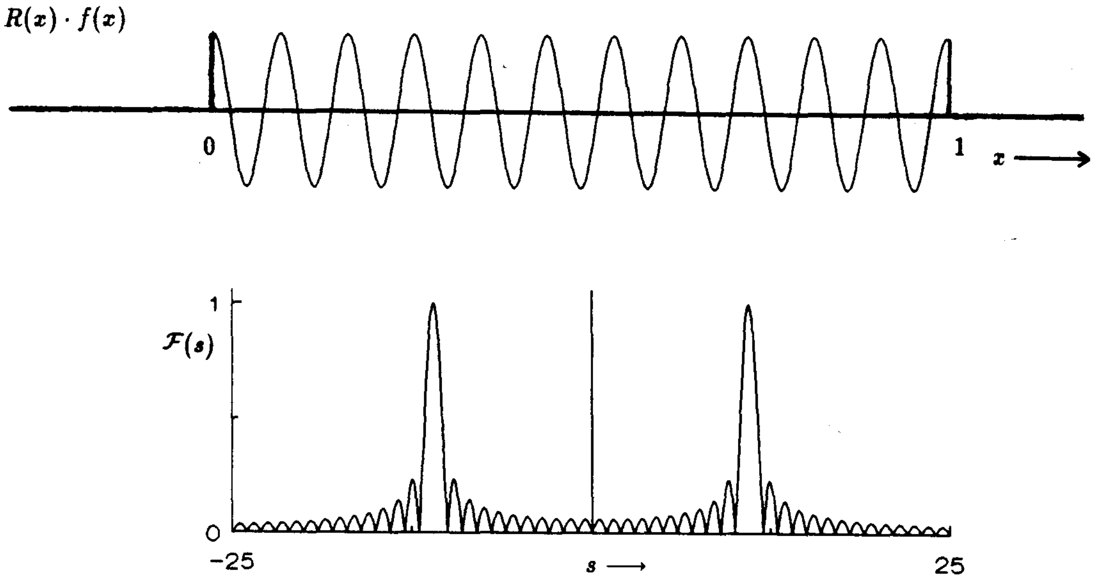

Figure 3.5 The upper graph shows the function $f(x) = \cos(2\pi x s_0)$ with $s_0 = 11$. The lower graph shows the corresponding continuous Fourier transform $\mathcal{F}(s)$. The difference from the two expected delta functions at $s = \pm 11$ results from x-domain truncation. The following parameters were used: $N\Delta x = 1.0$ and $\Delta s = 1.0$

A rectangular weighting function must be defined as:

$$R(x) = \begin{cases} 0 & \text{for } x < x_{min} \vee x > x_{min} + N\Delta x \\ 1/2 & \text{for } x = x_{min} \vee x = x_{min} + N\Delta x \\ 1 & \text{for } x_{min} < x < x_{min} + N\Delta x \end{cases} \tag{3.54}$$

For the time being we will assume that N is constant ($N = 64$). To demonstrate the effect of multiplying a data function $f(x)$ with a rectangular weighting function $R(x)$ one first has to look at the continuous Fourier transform of the function $R(x) \cdot f(x)$ (for simplicity we take $f(x) = \cos(2\pi s_0 x)$). This is visualized in figure 3.5. The s-domain is now continuous since we can't use the relation $f(y + N\Delta x) = f(y)$ here. The difference between the continuous Fourier transform and FFT is that for FFT only N points are selected in both the data function as in the corresponding Fourier transform.

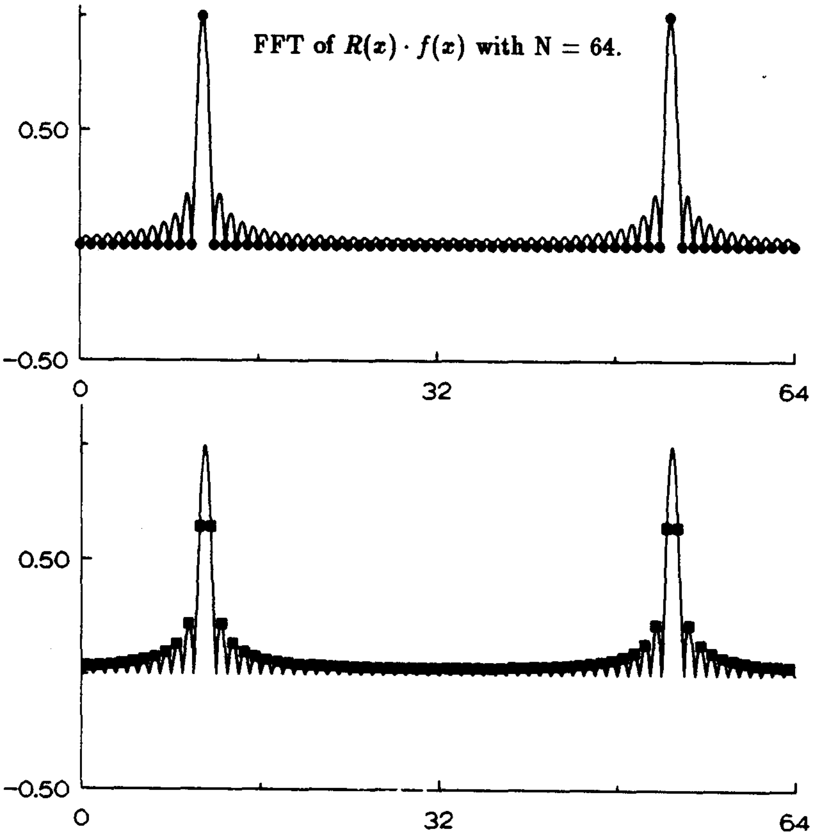

Figure 3.6 Obscured signal when a rectangular weighting function is used on a cosine function. From the continuous signal (—) only a discrete set of points is selected when an FFT is performed. Which N points are selected depends on the factor $s_0/\Delta s$. Here we display $s_0/\Delta s$ is integer (•) and $s_0/\Delta s$ is integer plus a half (■).

Notice that the continuous transform gives the same result as the FFT if we use the relation $f(y + N\Delta x) = f(y)$. The data points x_k are equally separated at a distance Δx while the Fourier spectrum is equally spaced at integer multiples of $\Delta s (= 1/(N\Delta x))$. Which N points in the frequency domain are selected from the continuous power spectrum depends on the number of periods, np ($= s_0/\Delta s$), on the interval $N\Delta x$. The two most interesting cases are illustrated in figure 3.6 where the dots represent the situation np_1 is integer and the squares represent the situation np_2 is integer plus a half. Note the apparent broadening (leakage) of the frequency peak at frequency s_0 for $np = np_2$ while for $np = np_1$ we have an almost delta peak at frequency s_0. This is the reason why the highest resolution is obtained when $N\Delta x$ is an integer multiple of the period. However if the period is an unknown parameter one can select a weighting function whose Fourier transform falls off more rapidly in amplitude on both sides of its peak value compared to the transform of a rectangular weighting function.

Characteristics of several weighting functions

Several weighting functions have been employed with the FFT. We'll discuss briefly the interesting features of the four most popular; the rectangular, the Hanning, the Parzen and the Bartlett window functions. These functions and their corresponding frequency response are defined in table 3.1 and depicted on the next page.

Table 3.1

x-domain here $z = \frac{x}{N\Delta x}$	s-domain	Highest side lobe dB	3 dB band width
$w_R(z) = \begin{cases} 1 & \lvert z\rvert \le \frac{1}{2} \\ 0 & \lvert z\rvert > \frac{1}{2} \end{cases}$	$w_R(s) = N\Delta x \cdot \mathrm{sinc}(\pi s N\Delta x)$	-13	$\frac{0.85}{N\Delta x}$
$w_B(z) = \begin{cases} 1 - \frac{z}{2} & \lvert z\rvert \le \frac{1}{2} \\ 0 & \lvert z\rvert > \frac{1}{2} \end{cases}$	$w_B(s) = \frac{N\Delta x}{2}\mathrm{sinc}^2(\pi s N\Delta x/2)$	-26	$\frac{1.25}{N\Delta x}$
$w_H(z) = \begin{cases} \cos^2(\pi z) & \lvert z\rvert \le \frac{1}{2} \\ 0 & \lvert z\rvert > \frac{1}{2} \end{cases}$	$w_H(s) = \frac{N\Delta x}{2}\frac{\mathrm{sinc}^2(\pi s N\Delta x)}{1-(sN\Delta x)^2}$	-32	$\frac{1.40}{N\Delta x}$
$w_P(z) = \begin{cases} 1 - 24z^2 + 48\lvert z\rvert^3 & \lvert z\rvert < \frac{1}{4} \\ 2(1 - 2\lvert z\rvert)^3 & \frac{1}{4} < \lvert z\rvert < \frac{1}{2} \\ 0 & \lvert z\rvert > \frac{1}{2} \end{cases}$	$w_P(s) = \frac{3N\Delta x}{8}\mathrm{sinc}^4(\pi s N\Delta x/4)$	-52	$\frac{1.82}{N\Delta x}$

All functions have sidelobes in the frequency domain but produce less leakage than the transform of the rectangular function. However they all have a broader main lobe. Recall that x-domain weighting is a frequency domain convolution so the broader the main lobe, the more smeared the results of the FFT become. In general, the more one reduces side lobes or leakage, the broader or more smeared the results of the FFT appear. One therefore should choose that weighting function whose characteristics are best suited to the problem being addressed. Whenever the technique of fast Fourier transformation is used to resolve periodic behaviour in a signal it is usually a matter of experimenting with various window functions until the window function is found which gives optimal results. In most cases however the Hanning weighting function gives a satisfactory result.

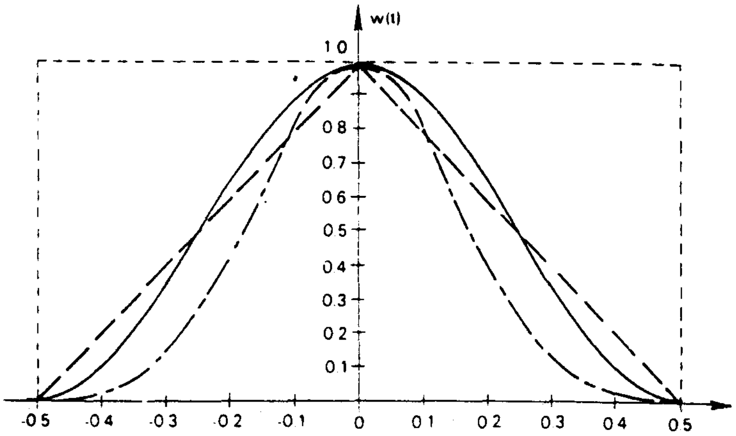

Figure 3.7 Four often used weighting functions.

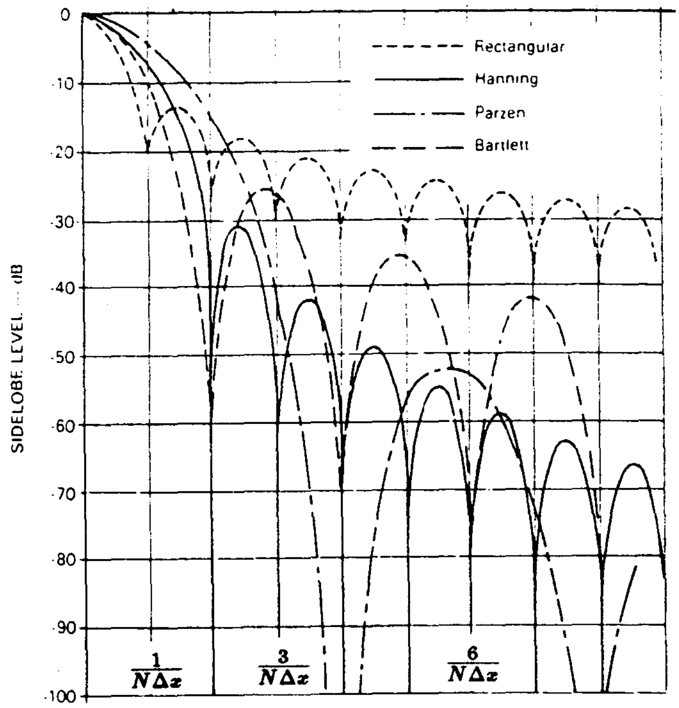

Figure 3.8 Absolute value of the Fourier transforms of the four weighting functions depicted in figure 3.7. The amplitude is expressed in dB's (read 20 $^{10}\log$).

SUMMARY

In this chapter the idea that the resistivity in a 2D electron gas acquires oscillatory components in a magnetic field is theoretically founded. According to this theory when using magnetic field modulation the measured signal has at least one periodicity in 1/B. If a high enough magnetic field is used ($\approx$ 20 Tesla) the different subband periodicities in δ-dopes can be found when applying a fast Fourier transformation on the signal in 1/B.

Chapter 4

Measurements on δ-dopes

In this chapter we present the results of measurements of six δ-doped samples grown in a computer controlled Varian Modular M.B.E. system at three different temperatures (480 $^{\circ}C$, 530 $^{\circ}C$, 620 $^{\circ}C$) with two different areal dopant concentrations of $2\ 10^{12}/cm^2$ and $8\ 10^{12}/cm^2$. The electrical characterization of the samples is presented in section one. The second section shows the experimental set-up of the magnetic field modulation measurements in fields up to 20 Tesla. All data has been recorded using a XT-PC and LAB-master$^{(20)}$. The results of the magnetic field modulated Shubnikov-de Haas measurements are presented in the following two sections. In section five we discuss the results of SIMS[1] measurements performed on two samples. We also performed cyclotron resonance measurements on two samples. These results will be discussed in section six. We will end this chapter with an evaluation of our measurements and compare the results and conclusions with publications of similar experiments.

4.1 Sample growth and electrical characterization

Our six δ-doped structures were grown in a computer controlled Varian Modular M.B.E. system using the following preperation menu: A substrate GaAs wafer is etched in order to remove possible (surface) polution. The final step of the etching procedure incorporates the creating of an oxide top layer on the substrate wafer, which later on will be thermally removed in the M.B.E. system [2]. After the oxide layer has been removed the actual growing menu for the δ-dopes can be started. First an initial 0.5 μm thick GaAs buffer layer was grown on the undoped (100) GaAs substrate at a temperature of $580^{\circ}C$ followed by a 2.5 μm GaAs layer at a substrate temperature T_{growth}. The latter temperature need not necessarily to be different from $580^{\circ}C$. We however have grown structures at substrate temperatures of $480^{\circ}C$, $530^{\circ}C$ and $620^{\circ}C$. To ensure a smooth surface the Ga-flux is interrupted 10 seconds

---

[1] Secondary Ion Mass Spectroscopy

[2] This is done at a temperature between 580° and $620^{\circ}C$ under a constant As-flux.

before the actual Si-atoms are deposited.

Sample	T_{growth} (^oC)	N_{Don} ($10^{12}/cm^2$)
A	480	2
B	530	2
C	620	2
D	480	8
E	530	8
F	620	8

Table 4.1 List of characteristic growing parameters of the samples.

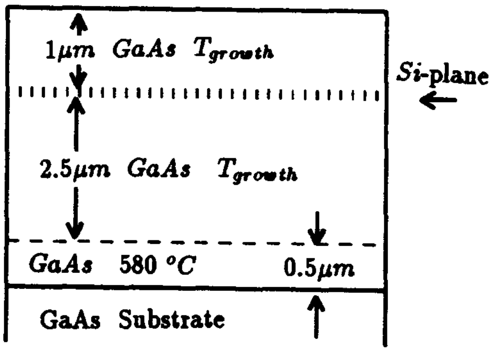

Figure 4.1 Schematic graph of the sample's structure.

The deposit of the donor atoms lasted only 7.5 or 30 seconds to obtain an areal donor density of 2 $10^{12}/cm^2$ or 8 $10^{12}/cm^2$ respectively. Finally a 1 μm thick GaAs top layer was grown at a temperature T_{growth}. A schematic diagram of the samples is shown in figure 4.1. Table 4.1 shows the characteristic growing parameters of all samples. The electrical characterization of the samples have been studied by Hall effect measurements using the Van der Pauw method. The Hall electron density n_{Hall} and the Hall mobility μ_{Hall} have been measured for temperatures between 4.2 and 300 K. These measurements are displayed in figures 4.2 and 4.3. The values at 4.2 K are also tabulated in table 4.2.

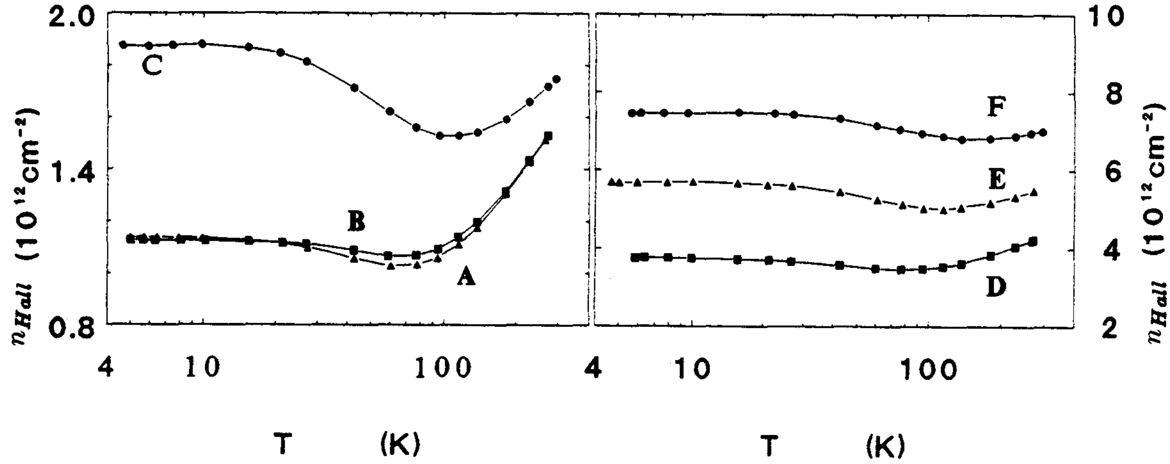

Figure 4.2 The measured temperature dependence of the Hall electron density n_{Hall} between 4.2 and 300 K.

An interesting result of figure 4.3 is the differences in mobility of the samples grown at 480°C and the one's grown at 620°C. This might indicate that the samples C & F have a more wide spread donor distribution function than the structures A & C. For temperatures below 77 K the most important scattering mechanism in δ-dopes is ionized impurity scattering so a smaller mobility certainly indicates a larger donor spread distance. A general difference between samples D, E and F and the set A, B and C is the slight temperature dependence of the heavily doped samples below 100 K. The influence of illumination (red LED) is also investigated by measuring again the Hall electron density and the Hall mobility as a function of the temperature. The results of the samples A,C,D and F are displayed in figure 4.4.

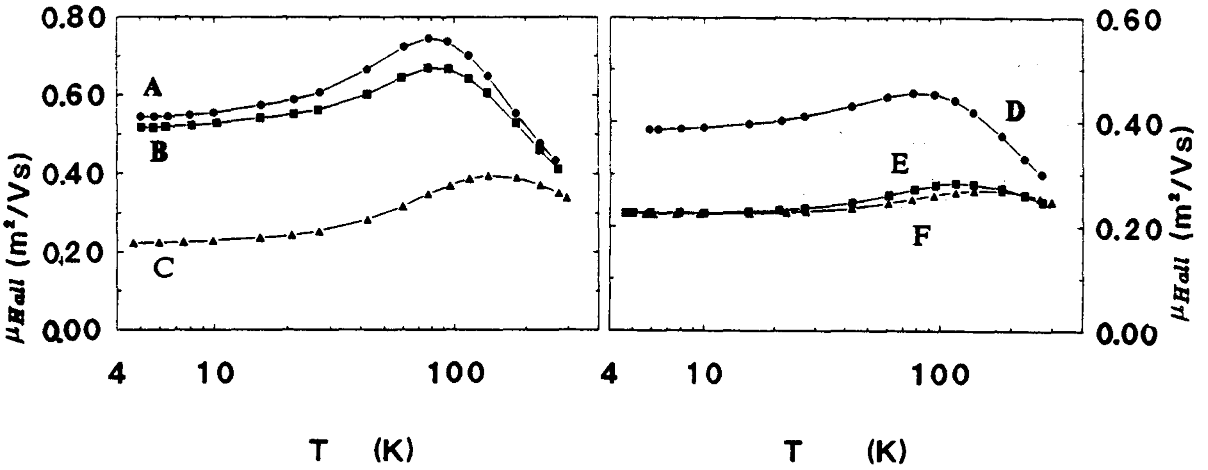

Figure 4.3 The measured temperature dependence of the Hall mobility μ_{Hall} between 4.2 and 300 K.

All samples show a decrease of the Hall electron density and an increase of the Hall mobility after illumination. The original as well as the illuminated samples have, for temperatures above 150 K, the same Hall mobility and Hall electron density.

Sample	n_{Hall} $(10^{12}/cm^2)$ dark	light	μ_{Hall} (m^2/Vs) dark	light
A	1.14	1.13	0.545	0.676
B	1.13	1.14	0.517	0.654
C	1.87	1.73	0.223	0.327
D	→ 3.76	3.27	0.385	0.515
E	5.70	5.05	0.226	0.280
F	7.46	7.30	0.224	0.243

Table 4.2 Table of Hall mobility and Hall electron density at 4.2 K before and after illumination.

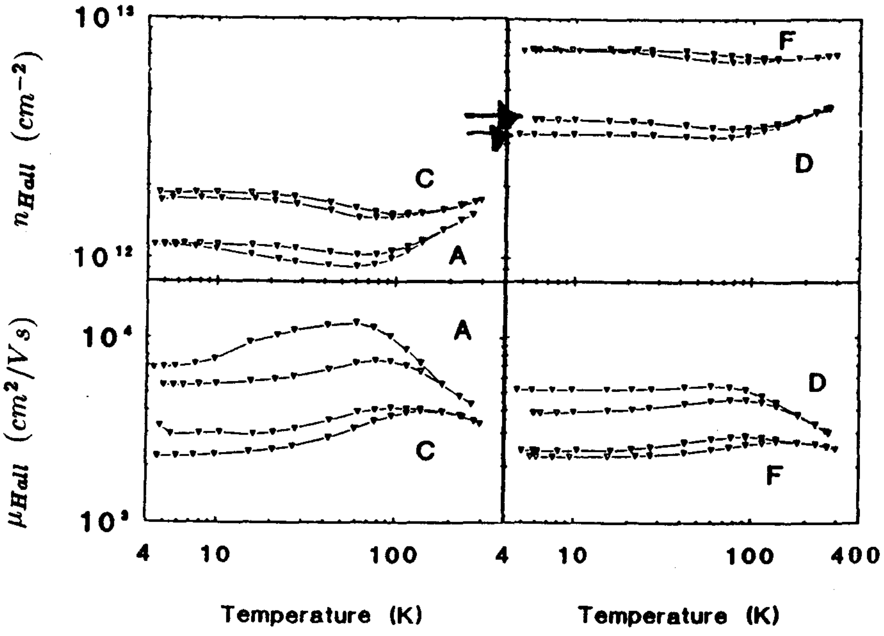

Figure 4.4 Measured temperature dependence of the Hall electron density and the Hall mobility between 4.2 and 300 K before (▽) and after illumination (▼).

4.2 Experimental set-up

The experimental set-up for the magnetic field modulated measurements is graphically displayed in figure 4.5. A sweepgenerator (SW) generates an in time slowly increasing and decreasing voltage V_{sw} which is proportional to the magnetic field. To this magnetic field controlling voltage a small oscillating (70 Hz) voltage V_f (Osc) is superimposed to create the modulating magnetic field B_{mod}. The voltage V_f also serves as reference signal for the Lock-ins (LI1 and LI2). The samples can be mounted on an insert which is placed in a He-bath in the center of the bitter magnetic system. This magnetic system generates fields up to 20 Tesla. Lowering the pressure above the He-bath enables measurements at temperatures between 4.2 and 1.2 K. A constant current I_{prep} ($\approx 100\mu A$) is sent through sample (S) contacts 1 and 5[3]. The Hall and Shubnikov-de Haas voltages are measured via Lock-in 1 and 2 respectively. The Lock-in output signals V_1 and V_2 now are proportional to the f (and/or 2f) harmonic parts of the Hall and the Shubnikov-de Haas voltages. These signals are plotted on a XY-recorder and written to data-files as a function of the magnetic field. All measurements were performed on Hall-bar structures. The precise geometry and size of the Hall-bar structures is displayed in appendix C.

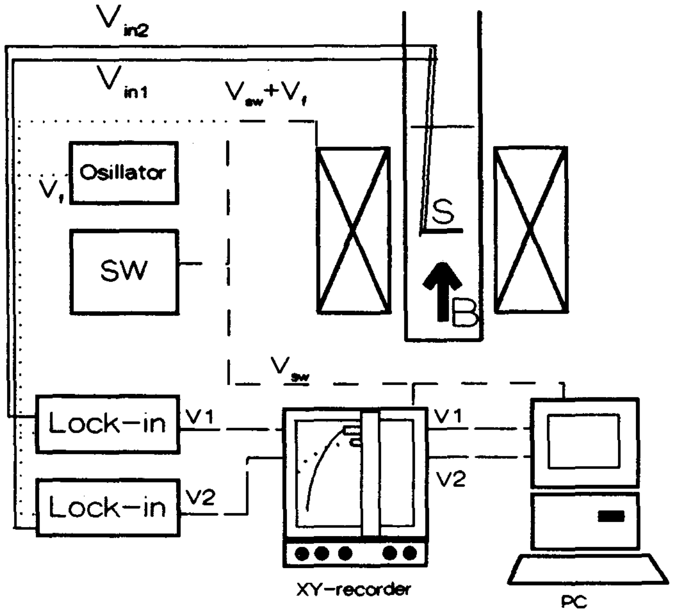

Figure 4.5 Schematic diagram of the experimental set-up used for the magnetic field modulated measurements.

The hard- and software(20) concerning the data transfer to the PC is specifically developed for field modulation measurements. In appendix D a short guidance to the program FFT19 is given. This program covers all mathematical action necessary to extract the periodicity in 1/B of the measured data.

---

[3] For sample contact definition see appendix C

4.3 Subband population measurements in perpendicular field

The population of the subbands has been determined from Shubnikov-de Haas and Hall effect measurements on Hall-bar shaped samples in magnetic fields up to 20 Tesla. To obtain a better resolution of the oscillatory parts in ρ_{xx} and ρ_{xy} the technique of magnetic field modulation was used with a modulation field of 30 mT at a modulation frequency of 70 Hz.

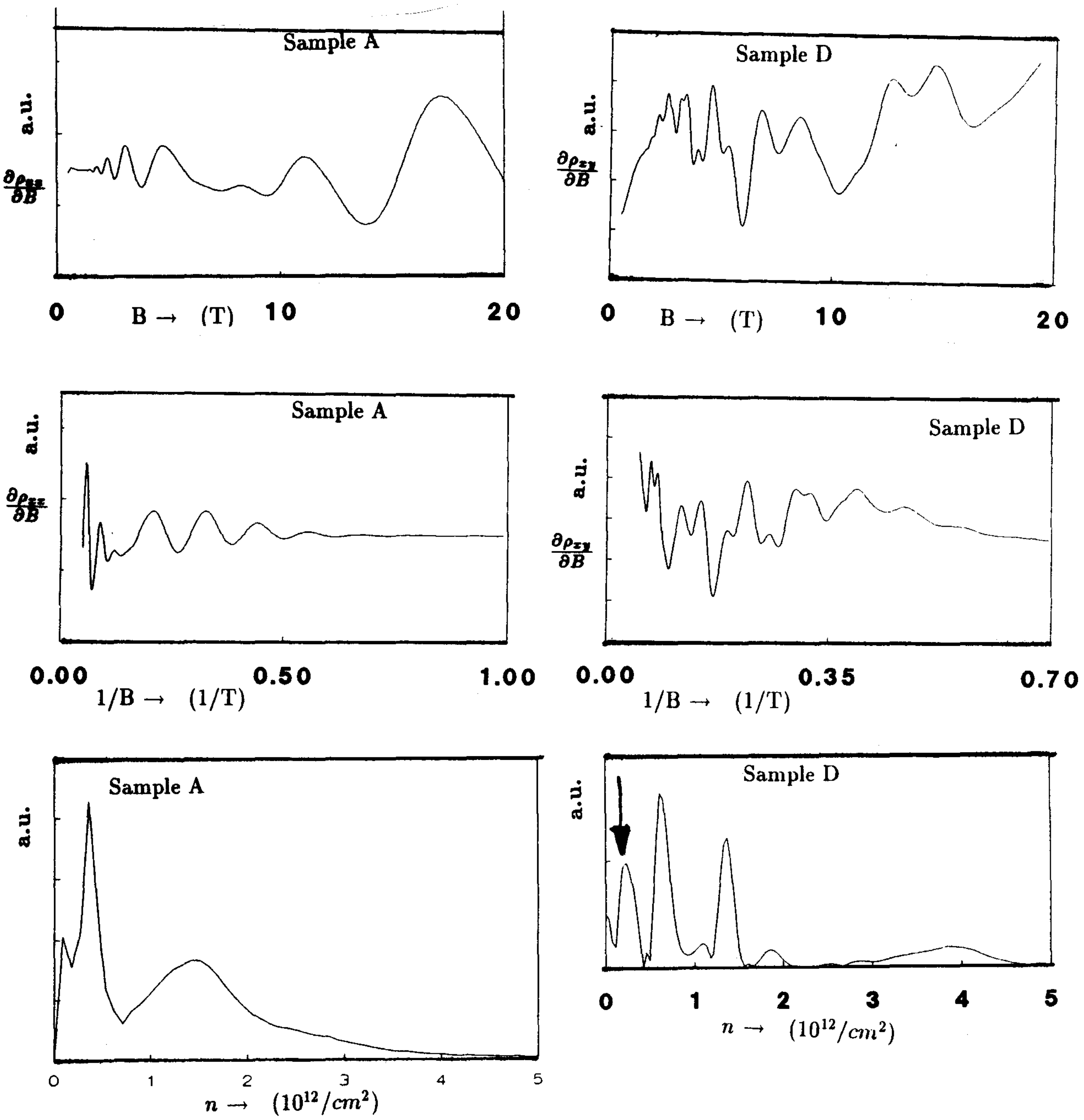

Figure 4.6 Example of typical results of measurements. Here samples at a growth temperature of 480°C are shown. In order to resolve the smallest periodicity the sample D we tilted this sample over an angle $\phi = 25.84°$. The x-axis of the Fourier transform of this sample hence must be multiplied with $\cos(\phi) = 0.9$ to get the proper subband populations.

This enables us to measure signals closely related[4] to $d\rho_{xx}/dB$ and $d\rho_{xy}/dB$. Taking the fast Fourier transform of these signals in 1/B gives the periodicities P_i of the different subbands. The periodicity however is proportional to the inverse of the subband population n_i via relation 3.37. Results of samples A and D are visualized in figure 4.6. Some extra figures of Fourier transforms of the other samples are collected in appendix E. Most measurements were performed at 4.2 K since temperature lowering to 1.2 K gave no essential signal improvement. Tables 4.3 a and b show the results of the subband population measurements for the samples A, B and C before and after illumination. The similar results for the heavily doped samples D and E are displayed in table 4.4 a and b. Unfortunately we were not able to extract the different subband populations from sample F. However the also tabulated Hall electron density indicates that almost all silicon atoms must be ionized since n_{tot} must be larger than or equal to n_{Hall}. In the samples A, B and C the value n_{tot} differs slightly from the areal Si-density. This is probably due to the formation of a depletion region on both sides of the 2DEG. However the heavily doped samples D and E show a much larger discrepancy. Clearly some other mechanism must be responsible for the relatively low value of n_{tot}. Zrenner *et al.*$^{(21)}$ argued that at low values of T_{growth} the electron concentration is limited by the

	A		B		C	
T_{growth}	480 °C		530 °C		620 °C	
	ρ_{xx}	ρ_{xy}	ρ_{xx}	ρ_{xy}	ρ_{xx}	ρ_{xy}
n_1	0.34	0.36	0.38	0.38	0.42	0.42
n_0	1.43	1.44	1.38	1.32	1.32	1.38
n_{tot}	1.77	1.80	1.76	1.70	1.74	1.80
n_{Hall}	1.14		1.13		1.87	

	A		B		C	
T_{growth}	480 °C		530 °C		620 °C	
	ρ_{xx}	ρ_{xy}	ρ_{xx}	ρ_{xy}	ρ_{xx}	ρ_{xy}
n_1	0.45	0.42	0.38	??	0.44	0.45
n_0	1.50	1.53	1.40	??	1.40	1.34
n_{tot}	1.95	1.95	1.78	??	1.84	1.79
n_{Hall}	1.12		1.14		1.80	

Table 4.3 **This table shows the different subband populations of the samples with an areal Si-density of 2 $10^{12}/cm^2$. Lefthand table before illumination; righthand table after illumination.**

	D		E		F	
T_{growth}	480 °C		530 °C		620 °C	
	ρ_{xx}	ρ_{xy}	ρ_{xx}	ρ_{xy}	ρ_{xx}	ρ_{xy}
n_3			0.16	0.18	??	
n_2	0.51	0.52	0.70	0.74	??	
n_1	1.23	1.24	1.66	1.71	??	
n_0	3.50	3.50	3.22	3.35	??	
n_{tot}	5.24	5.26	5.74	5.98		
n_{Hall}	3.77		5.7		7.5	

	D		E		F	
T_{growth}	480 °C		530 °C		620 °C	
	ρ_{xx}	ρ_{xy}	ρ_{xx}	ρ_{xy}	ρ_{xx}	ρ_{xy}
n_3			0.25	0.29	??	
n_2	0.56	0.55	0.75	0.78	??	
n_1	1.29	1.30	1.80	1.78	??	
n_0	3.50	3.50	3.32	3.50	??	
n_{tot}	5.35	5.35	6.12	6.35		
n_{Hall}	3.3		5.1		7.3	

Table 4.4 **This table shows the different subband populations of the samples with an areal Si-density of 8 $10^{12}/cm^2$. Lefthand table before illumination; righthand table after illumination.**

---

[4] See section 3.2

population of the DX-center at 200 meV above the Γ-conduction band minimum, whilst at high growing temperatures auto-compensation occurs prior to DX-center population. However when assuming that population of the DX-center is the main electron saturation mechanism for sample A, we are not able to fit the measurements with theoretical calculations. An areal electron density of 5.3 $10^{12}/cm^2$ is to low to give a Fermi level of about 200 meV above the Γ-conduction band minimum. The fact that no PPC-effect was measured is also an arguement against the population of the DX-center. Beall *et al.*$^{(22)}$ argued that at high areal dopant densities donor saturation occurs because of Si-islands formation. These islands consist of electrically active (donor) as well as electrically inactive Si. They noticed an increase of the areal electron density after annealing δ-doped samples several times. Diffusion of the inactive Si-atoms (eventually causing them to become electrically active) seems the most likely explanation for the increase in n_{tot}. The diffusion of Si-atoms was measured via Secondary Ion Mass Spectroscopy. When looking at the samples D, E and F we see an increase in n_{tot} when the growing temperature is raised. This indicates that at higher temperatures more Si-atoms become electrically active. The mobility however decreases at higher values of T_{growth} which indicates a more wide spread donor distribution. Conclusively we can say that during sample growth, segregation of Si-atoms seems to be an important mechanism, determining not only the donor spread function but also the areal donor density in the samples.

For a two subband system it is possible to calculate the different subband mobilities μ_0 and μ_1 using the following low field formulae$^{(3)}$:

$$\sum_{i=0}^{Nbound-1} (\mu_i \frac{n_i}{n_{Hall}}) = \mu_{Hall} \tag{4.1}$$

$$\sum_{i=0}^{Nbound-1} \mu_i \frac{n_i}{n_{Hall}} (\mu_i - \mu_{Hall}) = 0 \tag{4.2}$$

The subband mobilities of samples A, B and C are calculated that way and tabulated in table 4.5. For systems with more than two subbands one can only find an estimation for the subband mobilities. The best approximations for the different subband mobilities of the heavily doped samples D are also tabulated in this table.

Table 4.5 Table showing the calculated subband mobilities in m^2/Vs.

	A	B	C	D
μ_{HAll}	0.55	0.52	0.22	0.39
μ_0	0.22	0.20	0.22	0.15
μ_1	0.93	0.85	0.22	≈0.55
μ_2				≈0.55

The calculated mobilities of the second subband of samples A and D are higher than other δ-dope subband mobilities reported so far$^{(7,14,21)}$. The enhancement of the mobility in the samples grown at low temperature, is most probably due to the smaller overlap between the donors and the electron wavefunction$^{(23)}$. Above 100 K the mobility in all subbands is equal because longitudinal optical phonon scattering is the main scattering mechanism. This scattering mechanism is less sensitive to the electron wavefunctions than ionized impurity scattering.

With the measured subband population values, tabulated in tables 4.3 and 4.4, we are able to find an optimal set of numerically calculated values of n_i, when using the donor spread distance as a fitting parameter. The results of this fit of samples A and D are illustrated in figure 4.7. The best fitting donor spread distance for these samples is 20 Å. The optimal d_{Don} values for the other samples are tabulated in table 4.6. This fitting procedure however is no longer very sensitive for variations in the fitting parameter d_{Don} for d_{Don}-values below 40 Å.

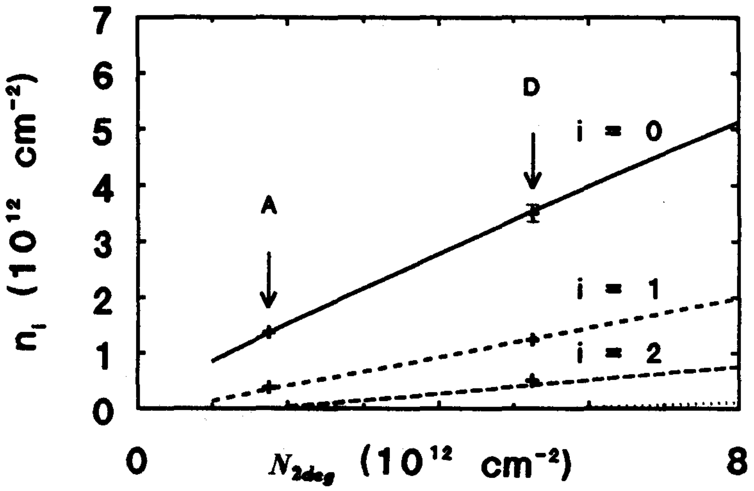

Figure 4.7 Figure showing the calculated and the measured subband population values of sample A and D. The best result is achieved with a donor spread distance of 20 Å.

	T_{growth}	D_{don}
A	480 ^oC	20 Å
B	530 ^oC	30 Å
C	620 ^oC	60 Å
D	480 ^oC	20 Å
E	530 ^oC	80 Å
F	620 ^oC	??

Table 4.6 Table showing the best fitting value of d_{Don} for the various samples. Sample F can not be related to some d_{Don} value because the different subband populations couldn't be determined.

An interesting result of this fitting procedure is the fact that the donor spread distance increases as the growth temperature of the samples is increased. This seems to substantiate the idea that at relatively high growth temperatures spreading of Si-atoms takes place and that the spreading depends on the areal Si-density.

4.4 Subband population measurements in tilted field

In the former section we investigated the influence of a perpendicular magnetic field on transport properties like the Hall and the Shubnikov-de Haas effect. The measured signals $d\rho_{xx}/dB$ and $d\rho_{xy}/dB$ finally give the different subband population values, n_i. With these values it is then possible to find a best fitting donor spread distance d_{Don}; meaning that we look for that particular value of d_{Don} which gives a minimum difference between the measured and numerically calculated subband population values. This can be done because the perpendicular magnetic field does not affect the shape of the potential function $U(z)$. However if there is also a magnetic field component parallel to the 2DEG, the total potential function becomes magnetic field dependent. In those situations we are no longer allowed to extract a d_{Don} value from the measured subband population values. Figure 4.8 shows the system's geometry in case the magnetic field is no longer perpendicular to the 2DEG. The perpendicular and parallel magnetic field components are Bcos(ϕ) and Bsin(ϕ) respectively.

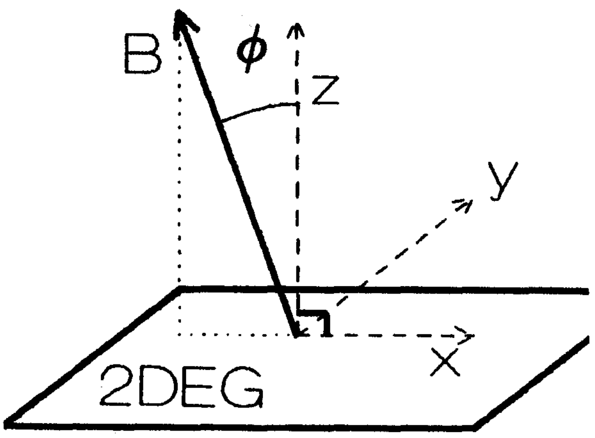

Figure 4.8 Geometry of the system in case the magnetic field is tilted over an angle ϕ.

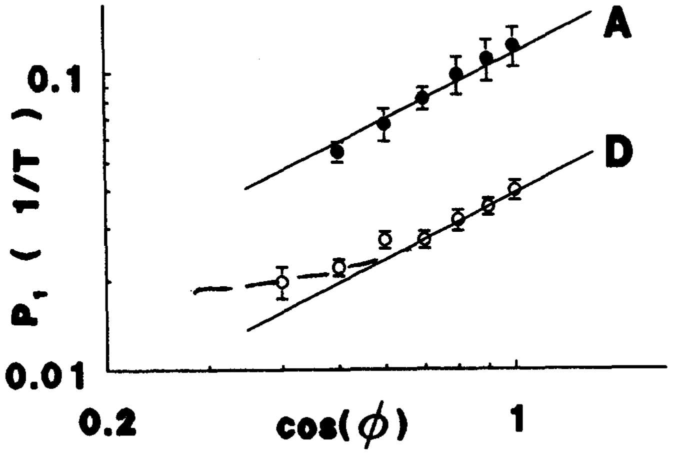

Figure 4.9 Measured value of P_1 (T^{-1}) as a function of cos(ϕ).

In order to investigate the influence of the parallel magnetic field component we measured the Shubnikov-de Haas and Hall signals and calculated the "corresponding" periodicities of the second subband, P_1. Figure 4.8 shows the functional dependency of the measured quantity P_1 and cos(ϕ) for the high mobility samples A and D. In case the parallel magnetic field does not affect the potential function of the system, we can expect a linear dependency $P_1 \sim \cos(\phi)$. CONST ? The line representing the linear situation is also drawn in figure 4.9. The population of the second subband of sample A (closed symbols) seems to be linear dependent on cos(ϕ) while sample D (open symbols) shows only a linear dependency on cos(ϕ) for small values of ϕ. For cos(ϕ) > 55° the relation $n_1/\cos(\phi)$ is a constant no longer holds. The cycltron radius of the electrons is the zx-plane is approximately 257Å $/\sqrt{B\sin(\phi)}$. Now if the cyclotron radius becomes of the same order as the "thickness" of the electron gas, the electrons can make circular orbits and the existence of the parallel magnetic field component is noticed. This could explain why sample D seems more affected be by the parallel magnetic field than sample A, since theoretical calculations show that the "thickness" of the electron gas increases for higher areal electron densities.

Further analyses need to be done on samples with various areal electron densities and at different growth temperatures ($\sim$ different value of d_{Don}) to show how the different subbands are affected by a parallel magnetic field component.

We also investigated the depopulation of the different subbands by measuring at parallel magnetic fields only. The Schrödinger equation of this system is

$$\{ \ (p_x^2 + p_y^2 + p_z^2)/2m^* + \frac{eB_{||}}{2m^*}(zp_x + p_xz) + \frac{e^2B_{||}^2z^2}{2m^*} + U(z) - E \ \}\Psi(x,y,z) = 0$$

This particular Schrödinger equation has been numerically solved by Reisinger$^{(24)}$ for a parabolic conduction band. The calculations gave the different subband energies as a function of $B_{||}$ and the areal electron concentration N_{2DEG} using a 5 Å broad donor distribution function. The calculated critical magnetic fields (magnetic field at which subband depopulation takes place) are visualized in figure 4.10 as a function of the areal electron density. First order perturbation theory shows that for a symetric potential U(z) the different subband energies E_n are lifted a factor dE_n, with

$$dE_n = < \Psi_n|z^2|\Psi_n > \frac{e^2 B_{\|}^2}{2m^*}$$

Clearly the higher subbands are more influenced because $< \Psi_n|z^2|\Psi_n >$ increases for higher subband indices. Eventually the highest subband will be lifted above the Fermi level (subband depopulation) and the electrons are rearranged over the remaining subbands. For higher magnetic fields the next subband will depopulate id. The resulting oscillations in the resistivity are called the diamagnetic SdH-effect.

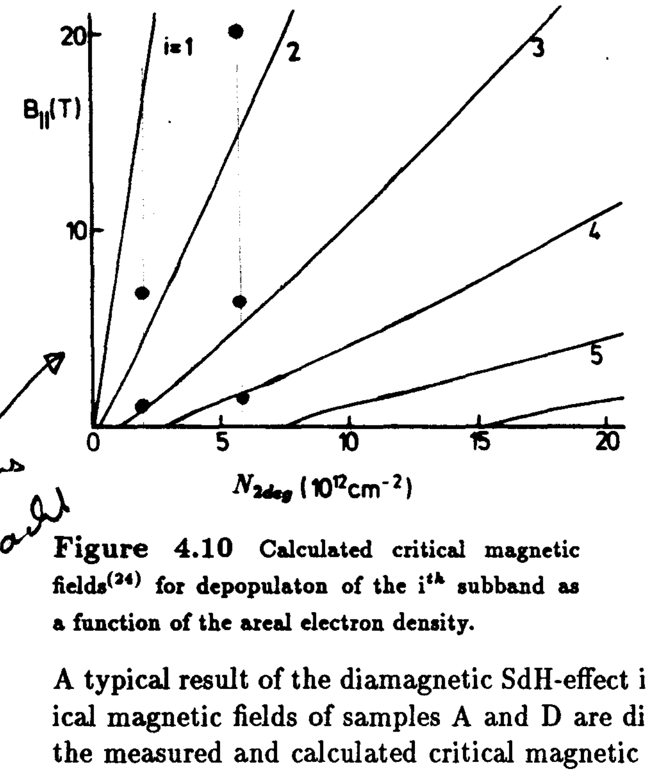

anders
als
vom [illegible]

Figure 4.10 Calculated critical magnetic fields(24) for depopulaton of the i^{th} subband as a function of the areal electron density.

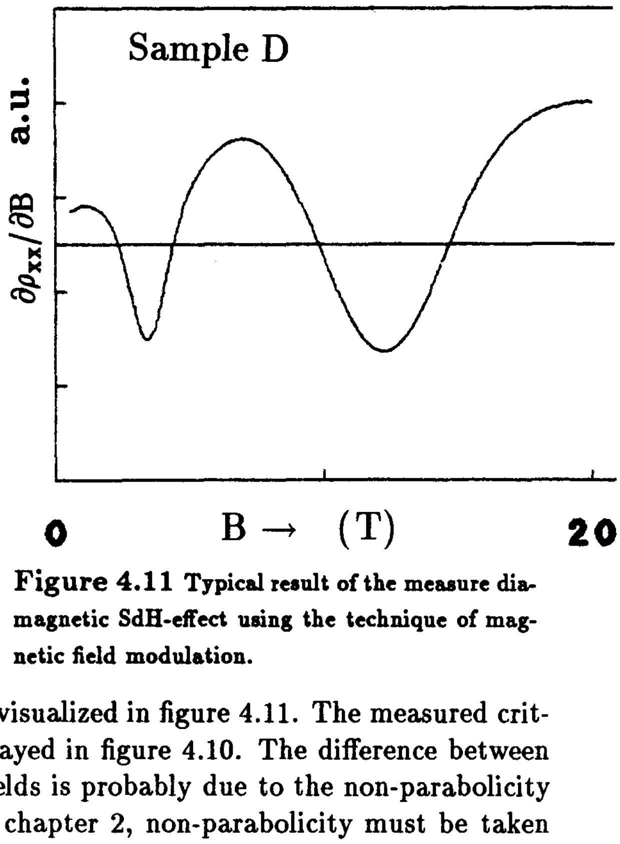

Figure 4.11 Typical result of the measure diamagnetic SdH-effect using the technique of magnetic field modulation.

A typical result of the diamagnetic SdH-effect is visualized in figure 4.11. The measured critical magnetic fields of samples A and D are diplayed in figure 4.10. The difference between the measured and calculated critical magnetic fields is probably due to the non-parabolicity of the conduction band in GaAs. As shown in chapter 2, non-parabolicity must be taken into account in the self-consistent calculations. Especially at small values of the donor spread distance, here $\leq 5\text{Å}$, non-parabolicity can give large corrections in system parameters like $E_f - E_i$. It would be very intersting to verify these data with a theoretical calculations which take non-parabolicity into account.

4.5 SIMS measurements

We performed SIMS (Secondary Ion Mass Spectroscopy) measurements on the samples D and F. With this technique it is possible to remove several atomic toplayers of a sample by shooting primary ions at the sample's surface and detect the (secondary) ions which are removed from the sample. This, however destructive technique, is very suitable for scanning the profile of samples in one direction and determine the chemical structure as a function of the depth. The resolution is about 3nm since not only one atomic toplayer is removed but a mixture of several atomic layers. The results of the SIMS measurements are displayed in figure 4.12. This figure shows that the sample grown at 620^0C has an asymmetric donor distribution function while sample D has a symmetric donor distribution. The asymmetry must be caused by segregation of Si-atoms during the growth of the sample.

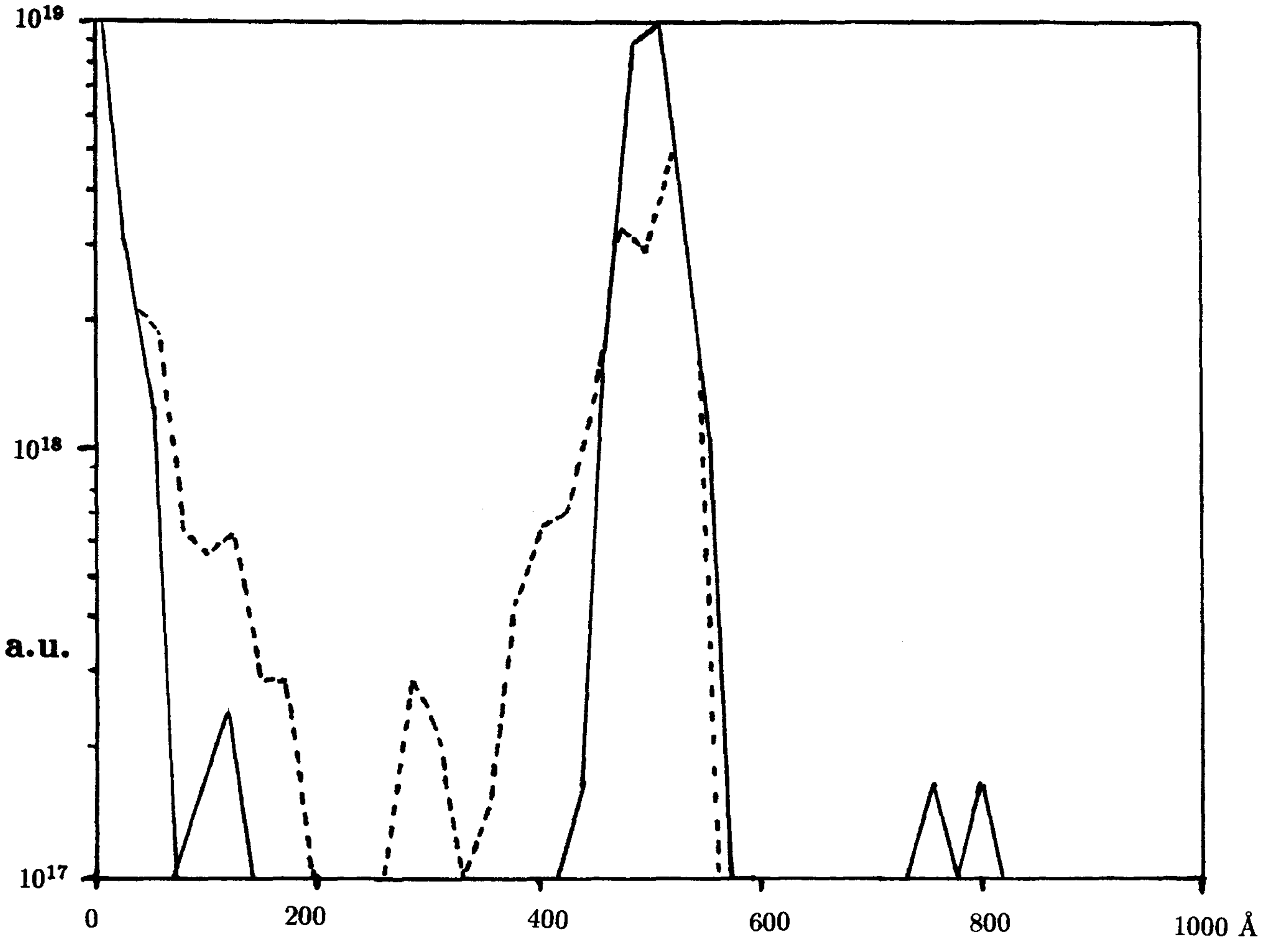

Figure 4.12 Si profile of the samples D (—) and F (- -) as a function of the etching depth.

The full width halve maximum values are 50 Å and 80 Å for samples D and F respectively. Conclusion: SIMS measurements show that segregation of Si-atoms takes place at a growth temperature of 620^oC. At a growth temperature of 480^oC these effects have disappeared. Further investigations need to be done to show the growth temperature dependency of the segregation effects. Diffusion of Si-atoms seems to be of minor importance in both samples.

4.6 Cyclotron resonance

The cyclotron resonance measurements are performed on the high mobility samples A and D. A schematic diagram of the experimental set-up is given in figure 4.13. We measured the transmission of the Far Infra Red laser light as a function of the magnetic field from 0 to 20 Tesla at a temperature of 1.3 K. A typical result of the measured transmission profiles is depicted in figure 4.14.

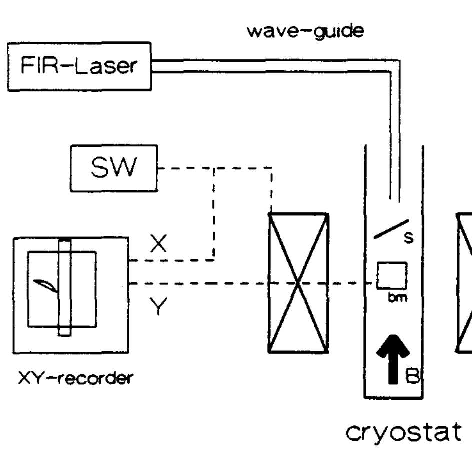

Figure 4.13 Experimental set-up of the measured FIR transmission profiles as a function of the magnetic field.
bm: bolometer; S: sample; SW: sweepgenerator and power supply for magnetic field.

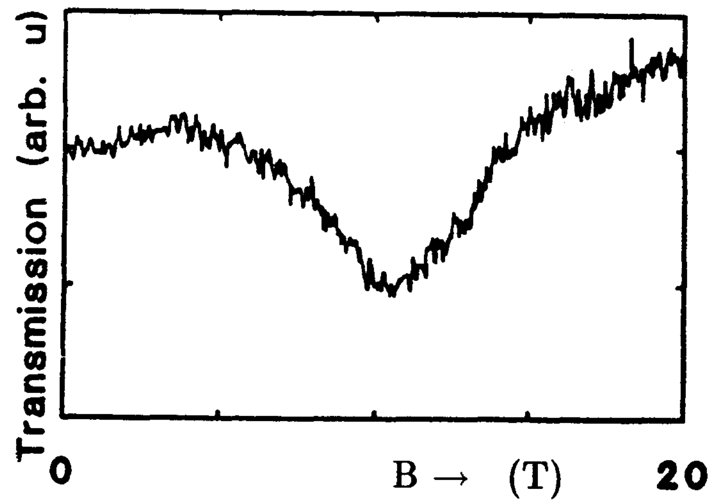

Figure 4.14 Typical result of a FIR transmission profile as a function of the magnetic field at a wavelength of 77.4 μm. The depth of the transmission dip is about 0.5% of the transmission signal.

The dips in the transmission profiles are all very broad. A reason for this extreme broadening can be the relatively low mobility (~ scattering time) of the δ-dopes compared to mobility of heterostructures. A second reason is the high areal electron density which gives rise to considerable dielectric broadening(25) of the CR-profile. Finally, as more than one subband is populated, the overlap of several less broad CR-profiles also give rise to an apparent broadening. Assuming the minimum of the transmission profiles is due to one subband we can determine an (cyclotron) effective mass m^*_{cycl} via the following equation:

$$m^*_{cycl} = \frac{e\ B_{min}\lambda}{2\pi c}$$

where λ is the laser wavelength; c the speed of light in vacuum; e is the proton charge and B_{min} is the value of the magnetic field at the minimum of the transmission profile. Figure 4.15 shows the calculated values of the cyclotron effective mass as a function of the laser wavelength λ for both the samples. The cyclotron effective mass differs considerably from the bulk GaAs effective mass $m^* = 0.067\ m_e$. The discrepancies are caused by the non-parabolicity of the conduction band in GaAs. It is easy to show that at low temperatures the cyclotron effective mass is proportional to the non-parabolic density of states function at the Fermi level $m^*_{cycl} = \pi\hbar^2 DOS_2(E_f)$. For large areal electron densities (large values of E_f) the relation between the cyclotron effective mass and the effective mass of bulk GaAs reads:

$m^*_{cycl} \approx 1.13\ m^*$ for sample A and $m^*_{cycl} \approx 1.26\ m^*$ for sample D .
Figure 4.15 shows that indeed the cyclotron effective mass is larger than the bulk effective mass value and that m^*_{cycl} in sample A is smaller than in sample D.

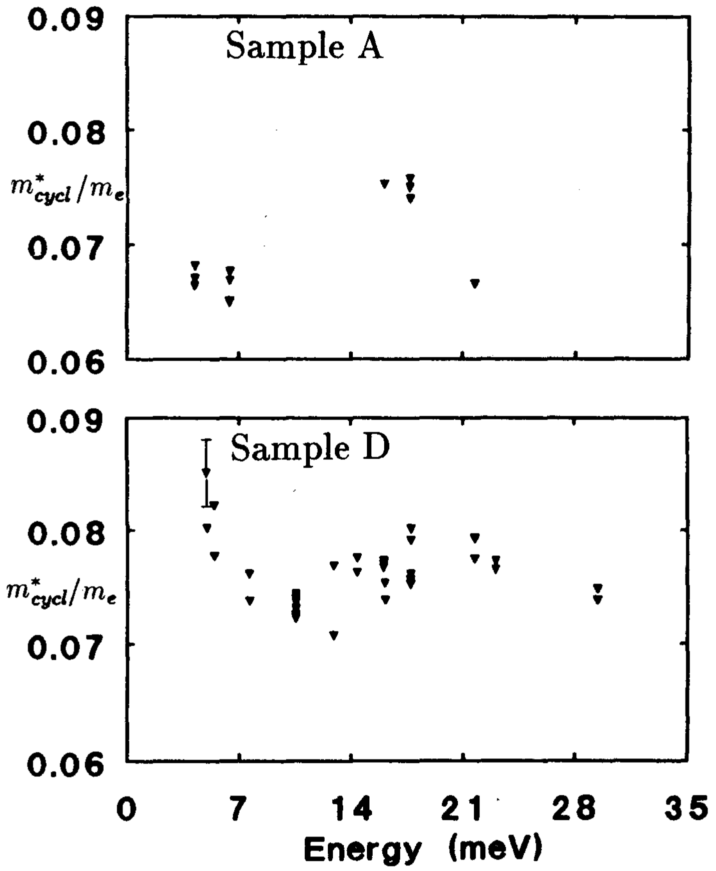

Figure 4.15 Measured cyclotron effective mass values as a function of the laser wavelength λ for sample A (upper) and sample D (lower).

It is not clear yet whether the measured transmission minima are wavelength dependent or just statistically scattered around a constant value.

4.7 Discussion

The growth temperature, T_{growth}, is a very important growing parameter for δ-doped structures. A relatively high value of T_{growth} brings about a more widely spread donor distribution function. The areal donor density is also an important system parameter that can limit the width of the donor spread distance. The most important mechanism that reduces the minimal value of the width of the dopant sheet seems to be the migration of Si-atoms with the growth front. Diffusion seems to be of minor importance during the growth. Magneto-transport measurements indicate that the samples grown at a temperature of $480°C$, have a donor with of 20 Å. For this value of T_{growth} the donor width is not influenced by the areal donor density, while at growth temperatures $\geq 520°C$, the donor spread distance becomes a function of both the areal donor density and the growth temperature. This latter conclusion is a little speculative since we only have performed measurements on a few samples. The same effects however have been noticed by Santos *et al.*(14)

The noticed discrepancy of the deposited areal Si-density and the measured value of electrically active Si-atoms in the heavily doped samples is still an unsolved effect. This effect reduces at higher growth temperatures. The most likely explanation is given by Beall *et al.*(22) who states that at sufficiently high dopant concentrations the Si-atoms will form clusters during the growth, which contain a relatively high concentration of electrically inactive Si. After annealing δ-doped samples, they noticed an increase in the number of electrically active Si-atoms. An other explanation for the noticed discrepancy was given by Zrenner *et al.*(21) who argued that at high areal electron densities the DX-center at $200meV$ above the Γ-band minimum is populated. This argument however fails for the heavily doped structure with a growth temperature of $480°C$ because no PPC-effect is measured. Furthermore, calculations show that an areal electron density of $5.3\ 10^{12}/cm^2$ can never give a Fermi level that is $200meV$ above the Γ-band minimum. The measured Hall mobilities of the samples grown at low temperature are much higher than mobilities reported so far. We were able to calculate the different subband mobilities for the lightly doped samples. The difference between the different subband mobilities is approximately a factor four for the samples grown at temperatures beneath $530°C$. In the high temperature grown sample the two subband mobilities are equal. This indicates a broader donor distribution function since the overlap of the subband wave functions with the ionized donors is closely related to the subband's mobility(23). The more the subband mobilities differ one another, the narrower the donor width must be.

We only used a symmetric charge distribution in all our numerical self-consistent calculations. Some of the δ-doped structures most certainly have an asymmetric donor distribution, due to Si-segregation during the growth. It is therefore recommendable to investigate the influence of asymmetric donor distributions on the system parameters. The presented set of calculations are still valuable since they can be used to calculated asymmetric systems via first order perturbation theory. The performance of numerical self-consistent calculations which allow asymmetric distributions, might be interesting. This however is an extremely time consuming job that should be given serious consideration to.

References

1. Zrenner A, (1987) Ph.D. thesis Technical University Munich
2. Slater J C, (1949) Phys. Rev. **76** 1592
3. Smith R A, (1978) -Semiconductors- Cambridge University Press Second edition
4. Kittel C, (1986) -Introduction to Solid State Physics- John Wiley & Sons, Inc. Sixth edition
5. Seeger K, (1982) -Semiconductor Physics An Introduction- Springer-Verlag Berlin Second edition
6. Hirakawa K, and Sakaki H, (1986) Phys. Rev. B **33** No. 12 8291
7. Gillman G, Vinter B, Barbier E, and Tardella A, (1988) Appl. Phys. Lett. **52** No. 12 972
8. Ploog K, (1987) J. Cryst. Growth **81** 304
9. Zrenner A, Koch F, and Ploog K, (1988) Surf. Sc. **196** 671
10. Voncken A P J, (1989) -Results of self-consistent calculations of Si-δ-doped GaAs- (Manual to the master thesis) University of Technology Eindhoven
11. Rössler U, (1984) Sol. St. Com. **49** No. 10 943
12. Gunnarson O, and Lundqvist B I, (1976) Phys. Rev. **B13** 4274
13. Voncken A P J, (1989) Probation report, University of Technology Eindhoven
14. Santos M, Sajoto T, Zrenner A, and Shayegan M, (1988) Appl. Phys. Lett. **53** No. 25 2504
15. Asher U, Mattheij R, and Russel R, (1988) -Numerical solutions of boundary value problems of ordinary differential equations- Englewood Cliffs. XXI Prentice-Hall
16. Beall R B, Clegg J B, Castagné J, and Harris J J, Semicond. Sci. Tech. to be published
17. Isihara A, Smrčka L, (1986) J. Phys. C **19** 6777
18. Das Sarma S, and Stern F, (1985) Phys. Rev. B **32** No. 12 8442
19. Brigham E O, (1988) -The Fast Fourier Transform and it's applications- Prentice Hall International Editions, Inc. First edition
20. Prins M, (1990) Master thesis, Technical University Eindhoven
21. Zrenner A, Koch F, Williams R L, Stradling R A, Ploog K,and Weimann G, (1988) Semicond. Sci. Tech. **3** 1203

22. Beall R B, Clegg J B, and Harris J J, (1988) Semicond. Sci. Tech. **3** 612

23. Shubert E F, Cunningham J E, and Tsang W T, (1987) Sol. St. Com. **63** 591

24. Reisinger H, and Koch F (1985) Proceedings of the 6th International Conference on Electronic Properties of Two-dimensional systems. Kyoto, 397

25. Langerak C J G M, Singleton J, v.d. Well P J, Pereboom J A A J, Barnes D J, Hopkins M A, Nicholas R J, and Foxon C T B, (1988) Phys. Rev. B **38** 13133

26. Stern F, and Das Sarma S, (1984) Phys. Rev. B **30** No. 2 840

Appendix A

Table of values

Quantity	Symbol	Value	SI
Velocity of light	c	2.997925	$10^8\ m\ s^{-1}$
Proton charge	e	1.60219	$10^{-19}\ C$
Planck's constant	h	6.62620	$10^{-34}\ J\ s$
	$\hbar$	1.05459	$10^{-34}\ J\ s$
Electron rest mass	m_e	9.10956	$10^{-31}\ kg$
Proton rest mass	m_p	1.67261	$10^{-27}\ kg$
Electron volt	eV	1.60219	$10^{-19}\ J$
Boltzmann constant	k_B	1.38062	$10^{-23}\ J\ K^{-1}$
Permittivity of free space	ϵ_0	8.8542	$10^{-12}\ F\ m^{-1}$
Permeability of free space	μ_0	1.2566	$10^{-6}\ H\ m^{-1}$
Bohr radius $\hbar^2/m_e e^2$	r_o	5.29177	$10^{-11}\ m$

Appendix B

The function that describes the number of electron states in the energy interval E and $E+\Delta E$ is called the density of states $DOS(E)$. This function can be calculated from the dispersion relation $E_{disp}(\mathbf{k})$ which gives a relation between energy E of the electrons and their wave vector $\mathbf{k} = (k_x, k_y, k_z)$. For a 3-D electron gas one can calculate the function $DOS_3(E)$ via the relation:

$$DOS_3(E)\Delta E = \sum_{\Delta k} 2$$

where the summation runs over all Δk combinations in k-space between the equi-energy surfaces $E = E_{disp}(k_x, k_y, k_z)$ and $E + \Delta E = E_{disp}(k_x + \Delta k_x, k_y + \Delta k_y, k_z + \Delta k_z)$. The summation can be rewritten as a volume integral of the density of states in k-space over the volume between surfaces E and $E + \Delta E$. So

$$DOS_3(E)dE = \iiint_{S_1}^{S2} 2(\tfrac{1}{2\pi})^3 d^3k$$

This can be written as

$$DOS_3(E) = \frac{d}{dE}\iiint_{S_1}^{S2} 2(\tfrac{1}{2\pi})^3 dS \frac{dE}{\|\nabla_{\mathbf{k}} E_{disp}\|}$$

where we used the relation: $d^3k = dS\frac{dE}{\|\nabla_{\mathbf{k}} E_{disp}\|}$ Finally the 3-D density of states can be written as an integral over an energy surface $S1$ in k-space weighted by the reciprocal of the function $\|\nabla_{\mathbf{k}} E_{disp}\|$.

$$DOS_3(E) = \iint_{S1} 2(\tfrac{1}{2\pi})^3 \frac{dS}{\|\nabla_{\mathbf{k}} E_{disp}\|}$$

For a two dimensional system the density of states can by calculated using the same procedure as above. This finally results in an integral over an energy curve $s1$ in the two dimensional k-space weighted by the reciprocal of the function $\|\nabla_{\mathbf{k}} E_{disp}\|$ given by

$$DOS_2(E) = \int_{S1} 2(\tfrac{1}{2\pi})^2 \frac{ds}{\|\nabla_{\mathbf{k}} E_{disp}\|}$$

With these formulae the density of states can be calculated even for an arbitrary dispersion relation. The dispersion relation for GaAs derived by Rössler(11) is a correction to the mostly used parabolic dispersion relation which is no longer valid at high electron concentrations. This non-parabolic dispersion relation is used to calculate the density of states $DOS_2(E)$ of a 2-D system like the δ-dopes.

Appendix C-1

The next three figure show the three Hall-bar types of the measured samples. All values are expressed in μm. The Hall-bar structure codes are 1^a, 2^a and 2^b.

Sample code	Hall-bar code
A	2^a
B	2^b
C	2^b
D	1^c
E	2^b
F	2^b

1^c

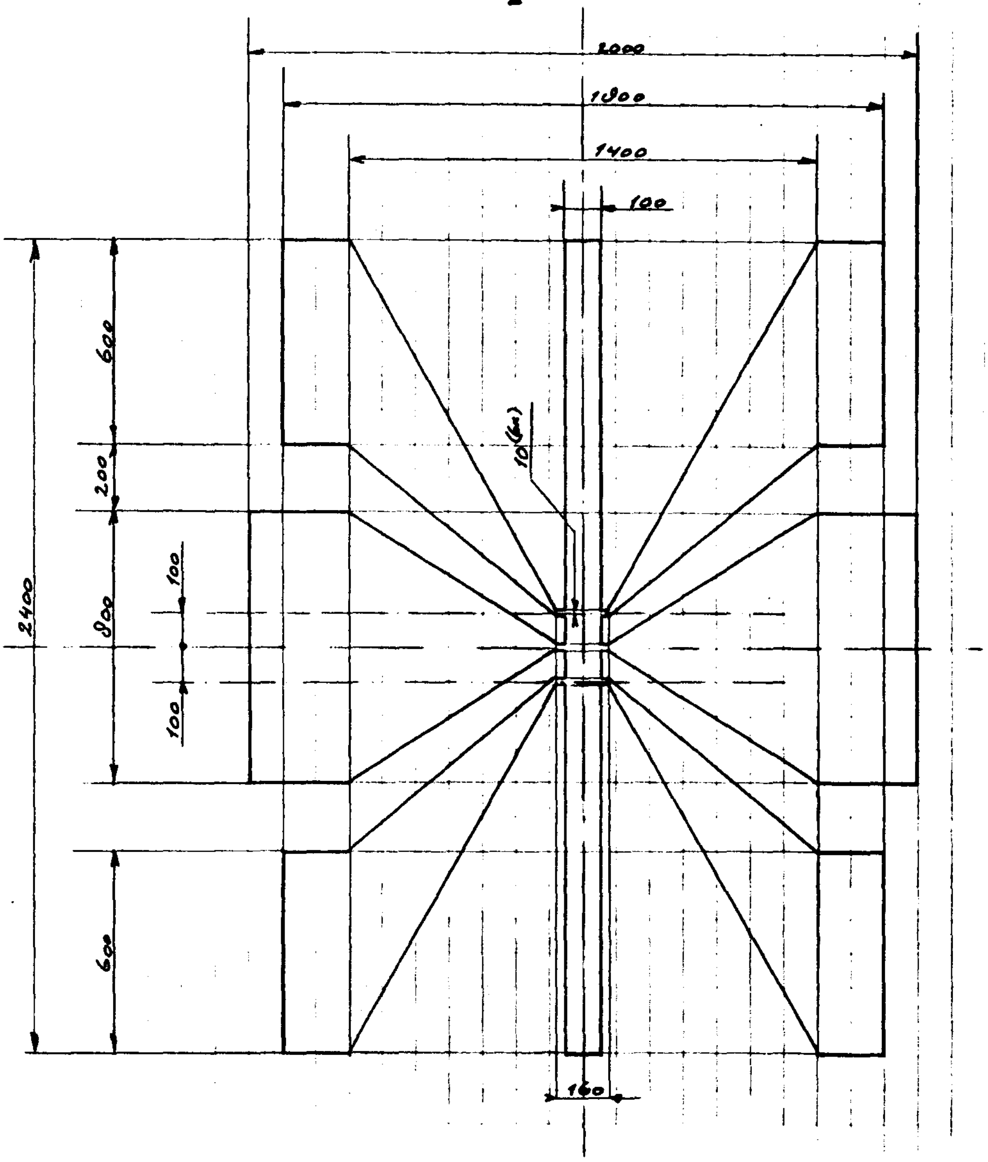

Appendix C-2

2b

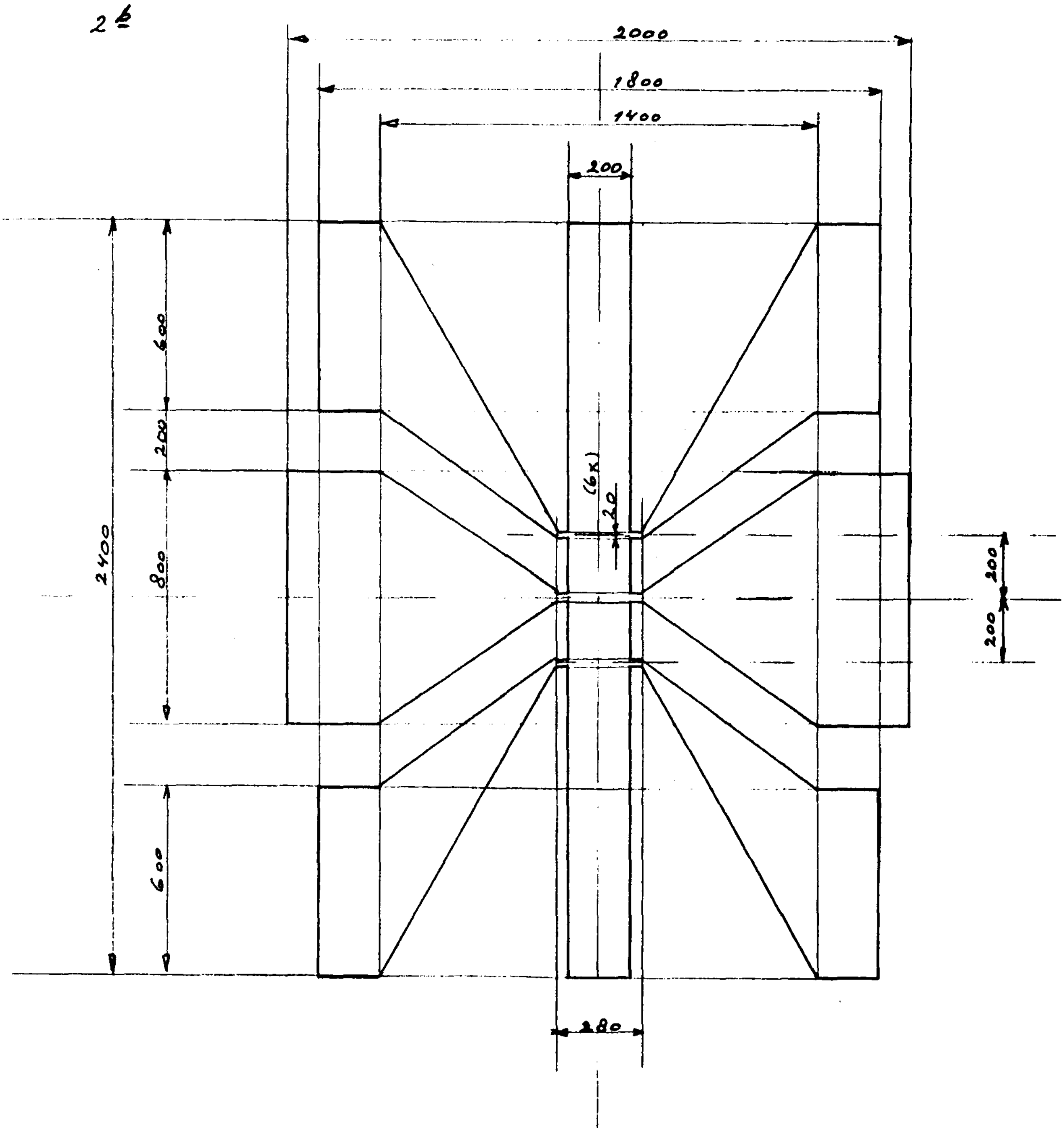

Appendix C-3

2a

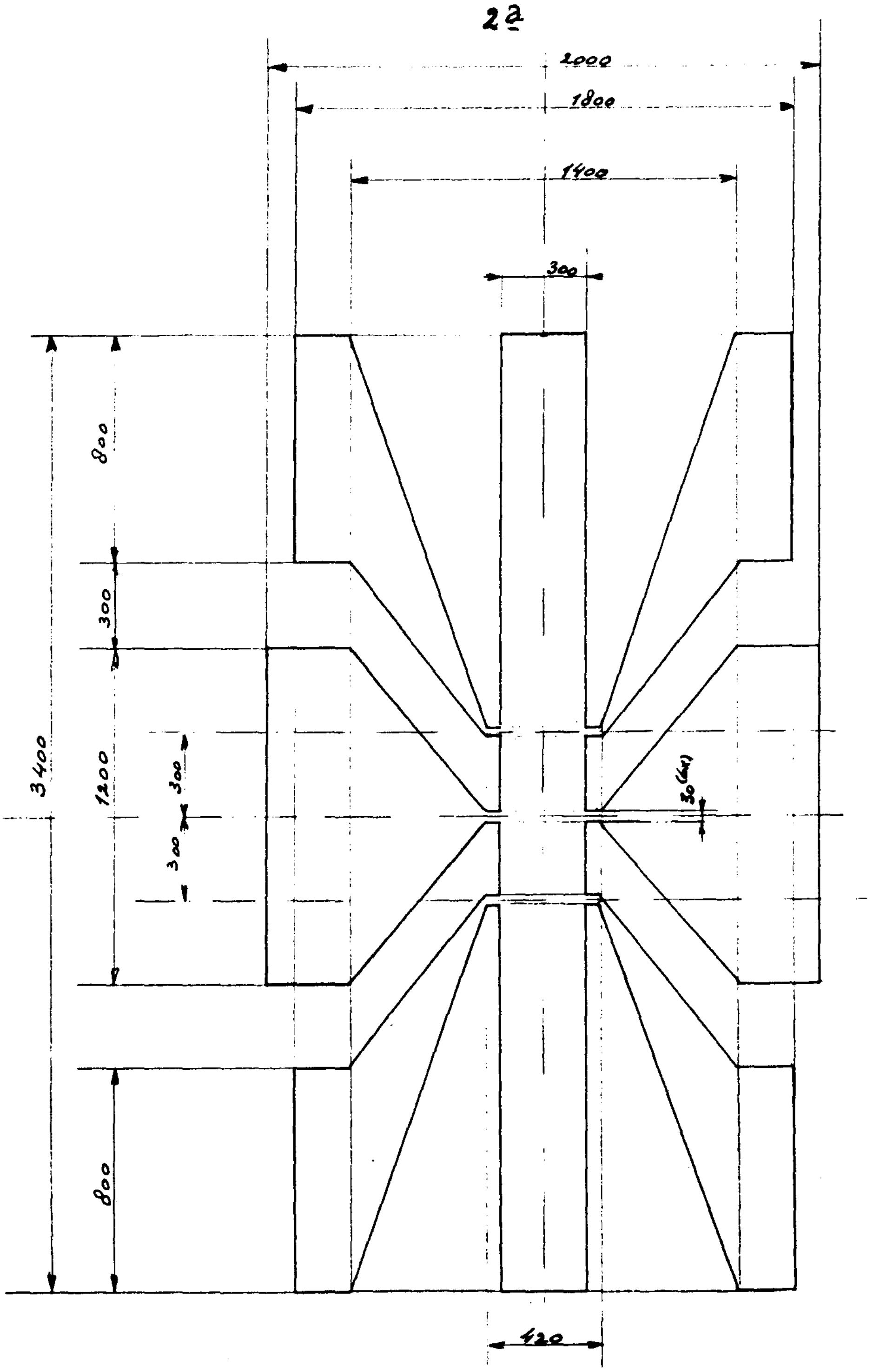

Appendix D-1

Short user guidance to the program FFT19

The program **FFT19** is an additional program to the measurement program **MAP**(20). It is written in **ASYST** (version 2) and can perform all the mathemetical actions necessary to extract the periodicities P_i and the corresponding subband populations n_i of the measured data. The program can be started on any DOS level by typing **FFT19**. When the program is loaded the (first-level) menu card is displayed with the following commands:

Option 0: Two types of data-files can be imported; Asyst files created with the program MAP and ASCII-files. The format of the latter file type should be:
-Line 1- Number of Y-data collumns (maximal value is 4).
-Line 2- Number of data rows to be read.
-Line 3 till end of file- lines with data.

Option 1: Only useful for (MAP)Asyst-files. This option clears the screen and shows the additional comment lines in the imported file.

Option 2: Shows the number of imported Y-channals (maximal is 4), and asks which channel should be plotted on screen. Both the original signal as the signal in 1/x are visualized. Use this option again to load another channel.

Option 3: This option asks whether you want to rescale the x-axis of the upper and/or the lower figure. Type 0 to leave an x-extrema unchanged.

Option 4: Enables one to write a small Y-label above both figures.

Option 5: Prints only the two visualized figures to the printer divice PRN.

Option 6: Option to alter the grid on/off condition.

Option 7: Option to enlarge figures only temporarely.

Option 8: Starts the FFT-menu and shows the FFT-menu card. The FFT-menu has 8-options which will be discussed next.

Option 9: Quit the program FFT19; Type start to restart the program or **bye** to return to DOS. The Crtl- Scroll Lock terminates the program at any program level. Type **SD** and hit enter to go to Asyst mode or **bye** to return to DOS.

Appendix D-2

FFT-menu commands

Option 1: Gives the absolute value of the Fast Fourier Transform of the imported data arrays. Two options can be used: FFT of Y(X) or FFT of Y(1/X).

Option 2: Advanced FFT option menu. Calculates the FFT of the signal using one of the following window functions; Rectandular, Cosine , Gauss or Triangle. Furthemore zero's can be added to the signal to "improve" resolution. With this option the signal is symmetrically mirrored in the maximum or minimum value of X; this improves the frequency resolution.

Option 3: Option to rescale the X-axis of the data.

Option 4: Option to rescale the X-axis of the calculated FFT.

Option 5: Option for saving signal arrays like original data and/or its calculated FFT.
-Line 1- Number of data-lines in file.
-Line 2 till end of file- X_i Y_i

Option 6: Prints the visualized graphs to the printer device PRN.

Option 7: Option to zoom in on the FFT signal only.

Option 8: Return to the main menu. FFT-data-arrays will be lost.

Appendix E-1

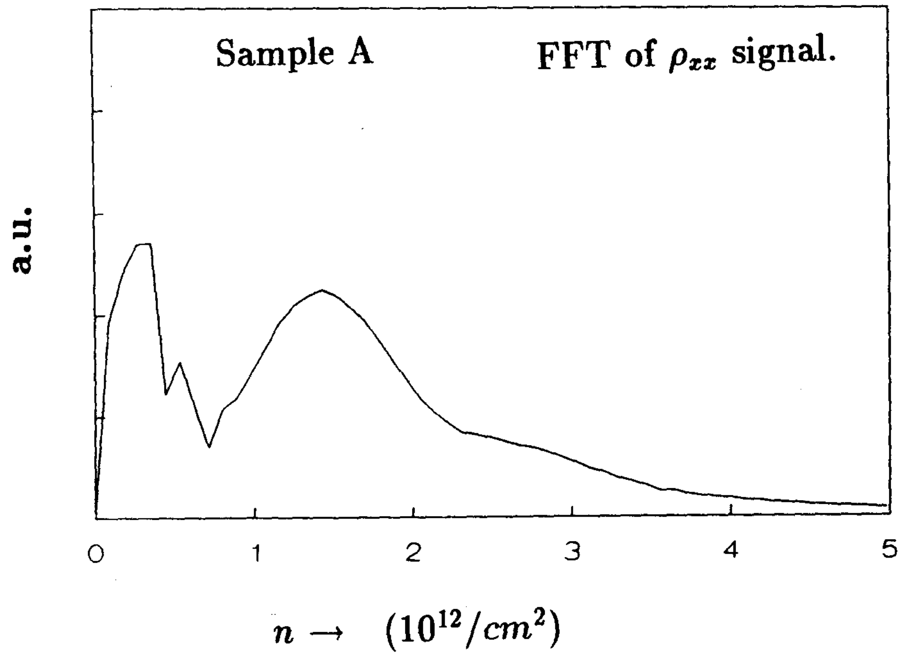
Sample A
FFT of ρ_{xx} signal.
a.u.
0
1
2
3
4
5
$n \rightarrow \quad (10^{12}/cm^2)$

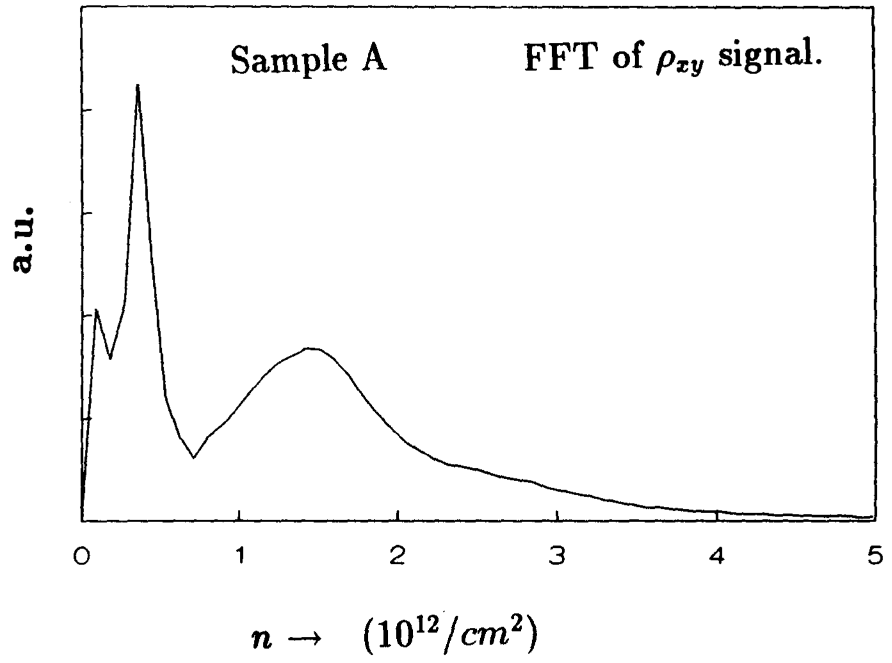
Sample A
FFT of ρ_{xy} signal.
a.u.
0
1
2
3
4
5
$n \rightarrow \quad (10^{12}/cm^2)$

Appendix E-2

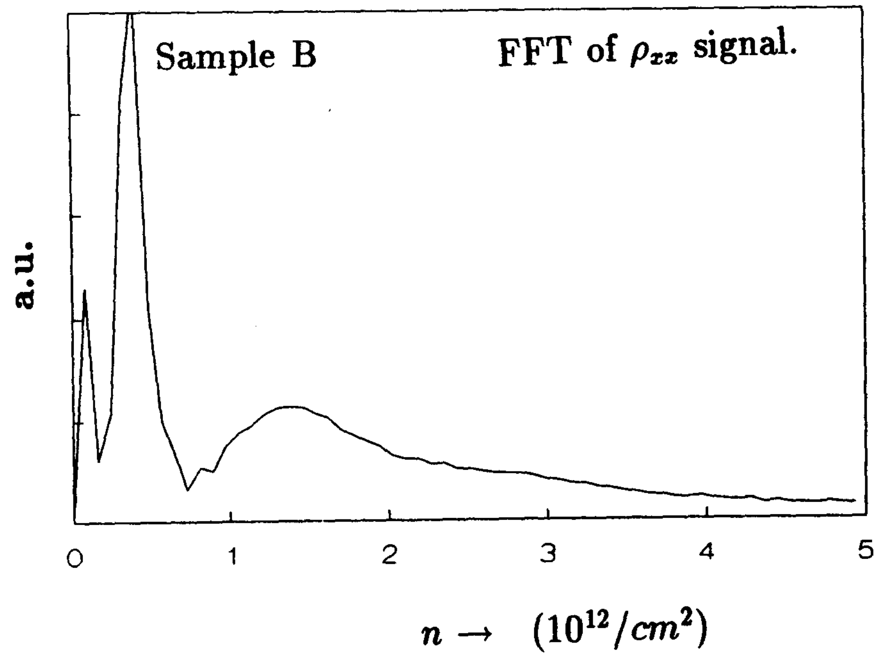
Sample B
FFT of ρ_{xx} signal.
a.u.
0
1
2
3
4
5
$n \rightarrow \quad (10^{12}/cm^2)$

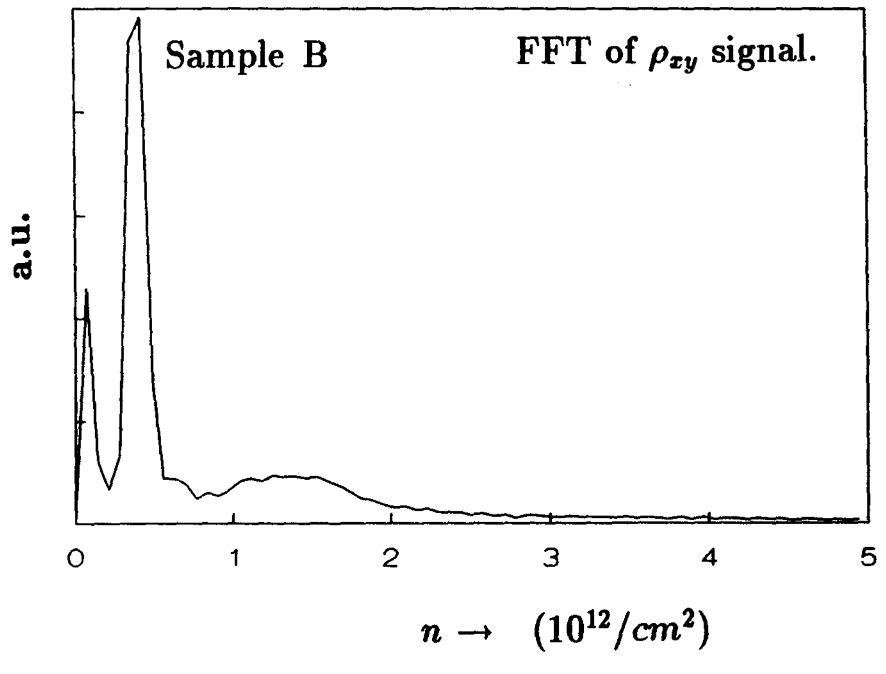
Sample B
FFT of ρ_{xy} signal.
a.u.
0
1
2
3
4
5
$n \rightarrow \quad (10^{12}/cm^2)$

Appendix E-3

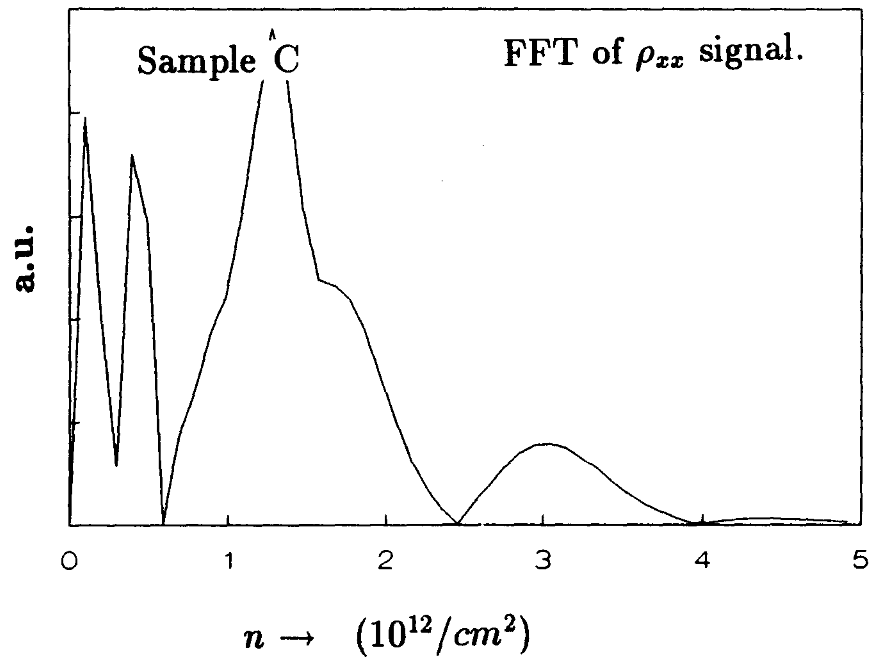
Sample C
FFT of ρ_{xx} signal.
a.u.
0
1
2
3
4
5
$n \rightarrow \quad (10^{12}/cm^2)$

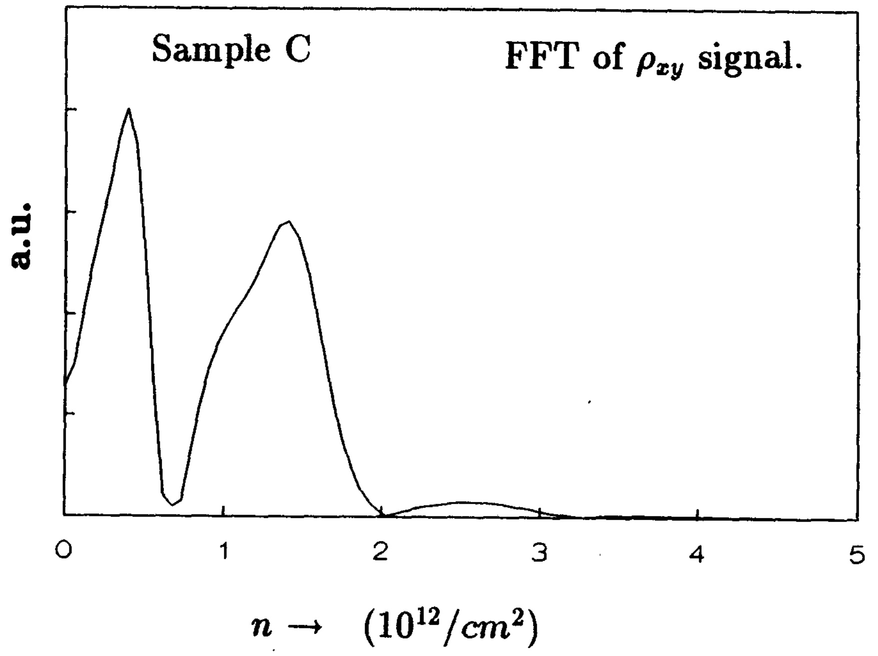
Sample C
FFT of ρ_{xy} signal.
a.u.
0
1
2
3
4
5
$n \rightarrow \quad (10^{12}/cm^2)$

Appendix E-4

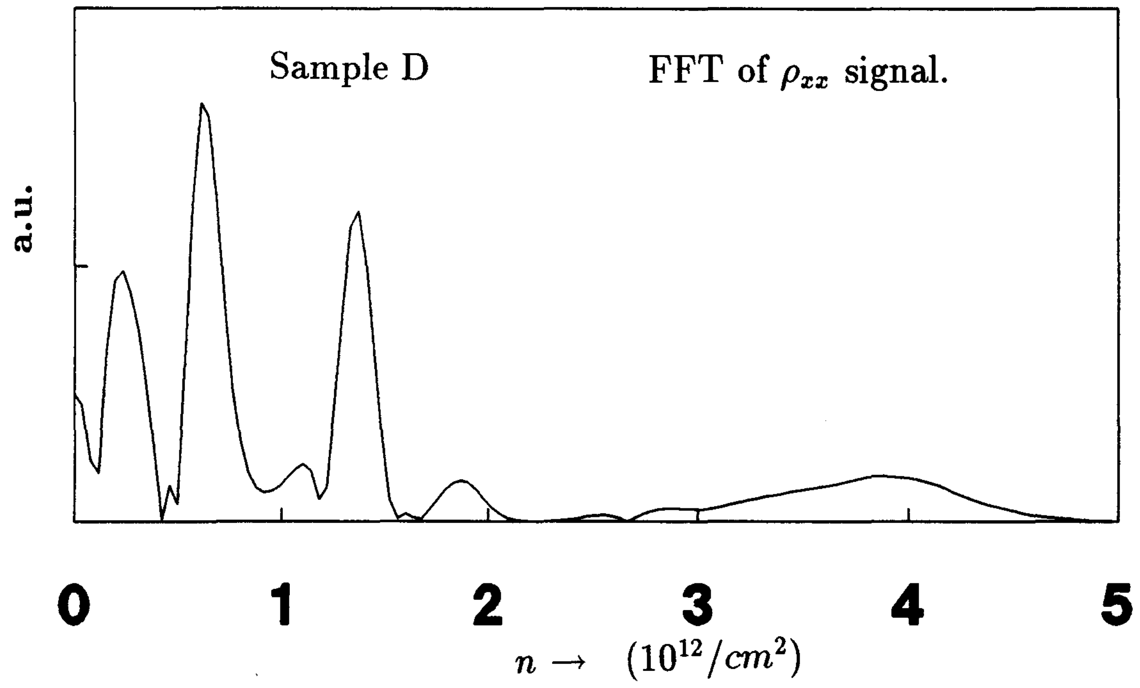

Appendix E-5

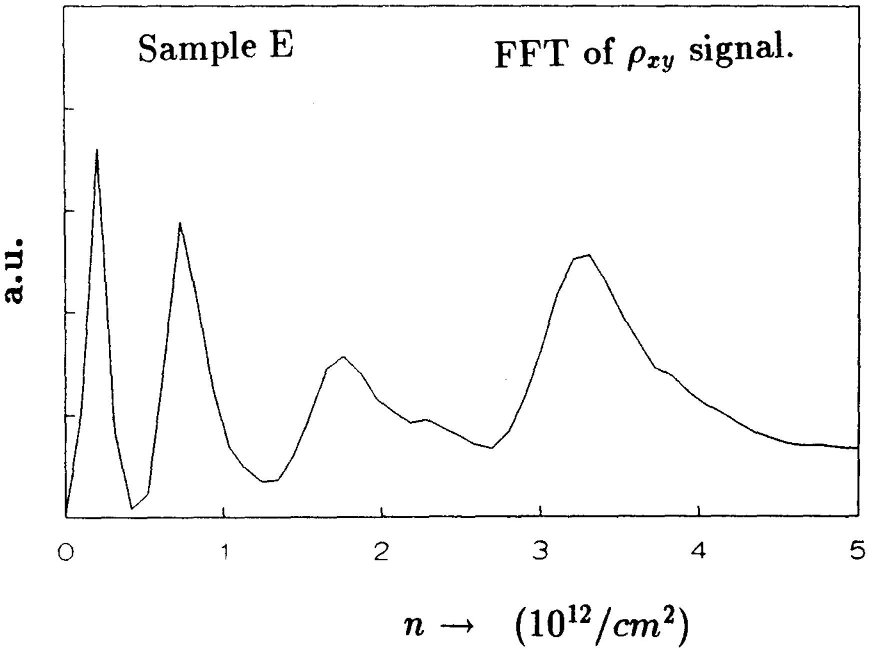
Sample E
FFT of ρ_{xy} signal.
a.u.
0
1
2
3
4
5
$n \rightarrow \quad (10^{12}/cm^2)$

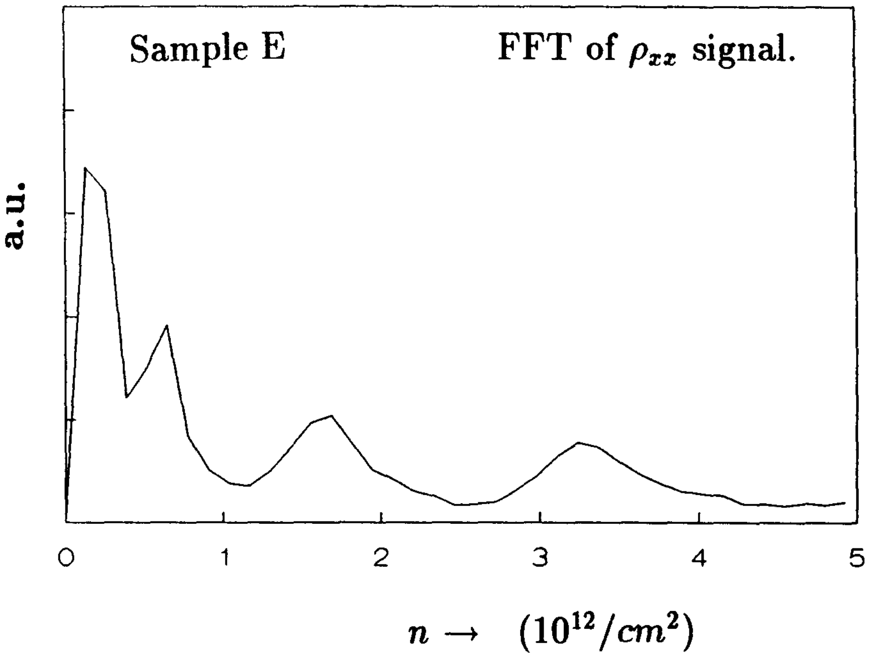
Sample E
FFT of ρ_{xx} signal.
a.u.
0
1
2
3
4
5
$n \rightarrow \quad (10^{12}/cm^2)$